Journal of Materials Chemistry A

ROYAL SOCIETY OF CHEMISTRY

REVIEW

View Article Online
View Journal | View Issue

Cite this: J. Mater. Chem. A, 2022, 10, 19444

Two-dimensional carbide/nitride (MXene) materials in thermal catalysis

Yuyao Yang, Yongqing Xu, Qinghai Li, Yanguo Zhang and Hui Zhou *

Received 29th April 2022
Accepted 11th July 2022

DOI: 10.1039/d2ta03481f

rsc.li/materials-a

Two-dimensional carbide/nitride materials, *i.e.*, MXenes, were first synthesized from the corresponding MAX phases in 2011. Since their discovery, they have been widely applied in batteries, supercapacitors, electromagnetic shielding materials, electrocatalysis, and photocatalysis due to their unique and tunable physical, chemical, and electrical properties. Recently, MXenes have been applied in thermal catalytic reactions, such as hydrogenation, dehydrogenation, water–gas shift reactions, and desulfurization due to their thermal stability and superior catalyst properties similar to noble metals. In this article, we systematically summarize the characteristics of MXenes as catalysts and supports compared with other traditional thermal catalysts with respect to both structures and catalytic activities. Furthermore, the nature of termination groups, active sites, and metal–MXene interactions are elaborated. Finally, we provide insights into the future development of catalysts based on MXene materials.

1. Introduction

Two-dimensional (2D) materials have unusual chemical and physical properties in contrast with traditional bulk materials due to their unique planar structures.[1–4] Therefore, increasing types of 2D materials with different structures and compositions were discovered, such as, graphene,[5,6] transition metal dichalcogenides (TMDs),[4,7] hexagonal boron nitride (h-BN),[3] layered double hydroxides (LDHs),[8] and 2D metal–organic frameworks (MOFs).[9] Among them, MXenes, first synthesized in 2011,[10–12] have gradually become the hot spot in the library of 2D materials. MXenes are two-dimensional transition metal carbides, carbonitrides, and nitrides with the general formula of $M_{n+1}X_nT_x$ ($n = 1$–3), where M is an early transition metal (such as Sc, Ti, Zr, Hf, V, Nb, Ta, Cr, and Mo), X is carbon and/or nitrogen, and T_x stands for surface terminations (hydroxyl, oxygen, or fluorine).[13–15] Till now, more than thirty kinds of MXenes with different stoichiometric compositions have been synthesized; countless possible solid solutions of MXenes have been designed theoretically; besides, plenty of new types are still under investigation.[16–18] Due to their diverse elemental compositions and adjustable surface terminations,[17,19] MXenes possess various interesting chemical and physical properties like a tunable bandgap,[1,20] good electrical conductivity,[21–24] excellent photoelectronic properties, and ultra-low optical attenuation.[25] Based on these superior features, MXenes play a significant role in many fields, such as energy storage and conversion,[26–28] sensors,[18,29] electromagnetic interference shielding,[30] absorption,[31] electrocatalysis,[32–34] and photocatalysis.[23,35,36] Recently, MXenes have also been sought-after in thermal catalysis, due to their tunable surface terminations and high thermal stability.[37,38] Moreover, it has been reported that MXenes have similar catalytic properties to noble metals.[39,40]

In thermal catalysis, MXenes can work as both catalysts and supports (Fig. 1). When MXenes serve as catalysts, they play a decisive role in many typical thermal reactions including hydrogenation,[16] dehydrogenation,[41] CO oxidation,[18,38] water–gas shift reaction,[42] and N_2 fixation,[43] in which $Ti_3(C/N)_2T_x$, Mo_2CT_x, and V_2CT_x are applied extensively.[44–46] When MXenes are used as supports, $Ti_3(C/N)_2T_x$ and Mo_2CT_x are widely used, and transition metals are loaded on them in the forms of nanoparticles (NPs),[47] nanoclusters (NCs),[48] or single atoms

Key Laboratory for Thermal Science and Power Engineering of Ministry of Education, Beijing Key Laboratory of CO_2 Utilization and Reduction Technology, Department of Energy and Power Engineering, Tsinghua University, Beijing 100084, P. R. China. E-mail: huizhou@tsinghua.edu.cn

Hui Zhou is an assistant professor at the Department of Energy and Power Engineering, Tsinghua University, China. His research interests include 2D materials, heterogeneous catalysis, bioenergy, and CO_2 utilization. He has published more than 60 peer-reviewed journal articles with more than 2500 citations. He was a Marie Curie Individual Fellow at ETH Zurich. He has also been awarded the Top Ten Rising Stars of Science and Technology of China. He is currently the Founding Associate Editor of Carbon Capture Science & Technology and the Associate Editor of Frontiers in Energy Research.

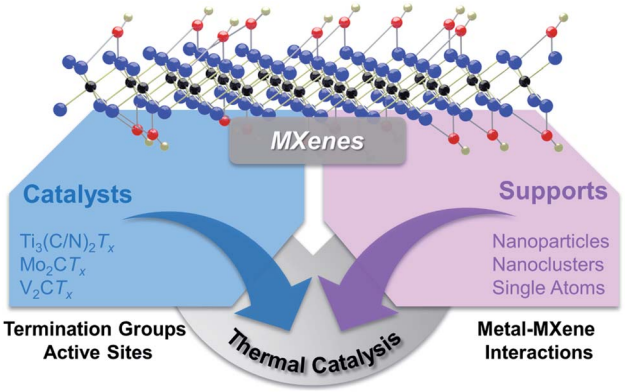

Fig. 1 The application of MXenes in thermal catalysis.

(SAs).[49] Moreover, to further enhance the catalytic performance,[50] some efforts, like surface functionalization,[51] heteroatom doping, and defect creation,[37] have also been made.[52]

This review summarizes the application of MXene materials in thermal heterogeneous catalysis. We discuss MXenes as both catalysts and supports, with an emphasis on the termination groups, active sites, and the interactions of MXenes with transition metals (Fig. 1). Finally, we discuss the future opportunities and challenges for MXene-based catalysts in this field.

2. Structure and synthesis of MXenes

2.1 Structure of MXenes

The structure of MXenes includes the $M_{n+1}X_n$ skeleton from the corresponding MAX phases (precursors of MXenes) and the interfacial termination groups from the specific synthetic process.[34] The MAX phases are layered ternary carbides and nitrides,[13] with the hexagonal structure of $M_{n+1}X_n$ units and alternately stacked A atoms (mainly elements of groups 13 and 14 of the periodic table, such as Al and Si).[25] In ceramic phases of MAX, the "M–X" interactions are mainly covalent and ionic bonds, whereas "M–A" bonds are metallic.[13] As shown in Fig. 2, MXenes inherit the hexagonal atomic lattice $P6_3/mmc$ from the MAX parent phase, in which the M atoms are hexagonally closed packed and X atoms fill the octahedral interstitial sites.[1] Through the change of n (Fig. 2(i)) in $M_{n+1}X_n$ units, $M_{1.33}X$, M_2X, M_3X_2, and M_4X_3 can be obtained. Moreover, by varying the type of M element in structural motifs (Fig. 2(ii)), solid-solution $M_{n+1}X_n$ units and o-$M_{n+1}X_n$ (a type of ordered MXene) are fabricated.[17]

Among mono-M MXenes, M atoms in the M_2XT_x phase follow ABABAB ordering corresponding to hexagonal close-packed stacking, whereas M atoms are face-centered cubic stacked with ABCABC ordering in $M_3C_2T_x$ and $M_4C_3T_x$ phases.[53] Recently, i-MXenes with the formula of $M_{1.33}XT_x$ were

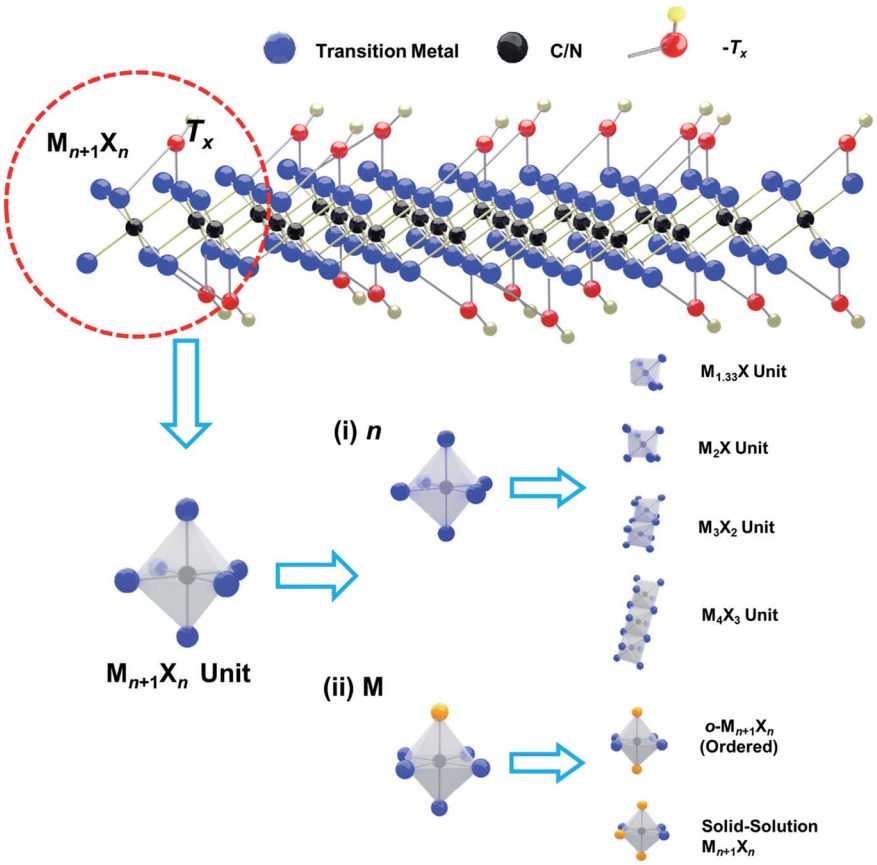

Fig. 2 The structure of MXenes with different $M_{n+1}X_n$ units and termination groups, where M refers to an early transition metal, X is carbon and/or nitrogen, and n stands for the number of X.

discovered. The materials have ordered vacancies and only one kind of M element dispersed in the basal plane.[54] Furthermore, MXenes contain two kinds of M elements in their components, which greatly expand their variety. More than ten kinds of double-M MXene phases have been synthesized and thousands have been predicted (Fig. 3). In the solid solution ($(M,M')_{n+1}C_nT_x$), M and M′ metal elements are randomly distributed throughout the entire structure,[17] and their electrochemical[55] and catalytic properties can be tuned by controlling the ratio of these two transition metal elements.[56] Up to now, many solid solutions, such as $(Ti,V)_2CT_x$, $(Ti,Nb)_2CT_x$, $(Mo,V)_4C_3T_x$, and $(Nb,Zr)_4C_3T_x$, have been synthesized; however, they account for only a small part of countless predicted phases.[17] As for ordered MXenes, o-MXenes are one of the most important types, where one or two layers of an M element are sandwiched between layers of another M element.[57] It has been reported that in synthesized o-MXenes, the outer layers are commonly occupied by Mo or Cr, while the center is occupied by Ti or V.[1]

In addition to the $M_{n+1}X_n$ skeletons, the electronegative termination groups, formed in the aqueous synthetic system, also play an important role in providing MXenes with excellent properties. To stabilize the MXenes, termination groups are usually located at three sites including (i) the top of the transition metal atoms, (ii) the hollow position between the top metal atoms, and (iii) the hollow position between the next stack of X atoms. Due to the low steric hindrance surface, terminations located at site (i) on both sides of MXene sheets are the most stable configuration for most MXenes according to density functional theory (DFT) calculations. However, site (ii) becomes more energetically favorable for MXenes when the transition metals cannot provide sufficient electrons to both X and surface terminations. For example, O-termination MXenes with low valency transition metals tend to be either in site (ii) configuration or mixed sites (i) and (ii), because two electrons are required to stabilize their adsorption position, but only one electron can be obtained from transition metal surface sites.[11] Furthermore, changing the coverage of surface termination groups can have an influence on the selectivity and activity of the reactions.[58]

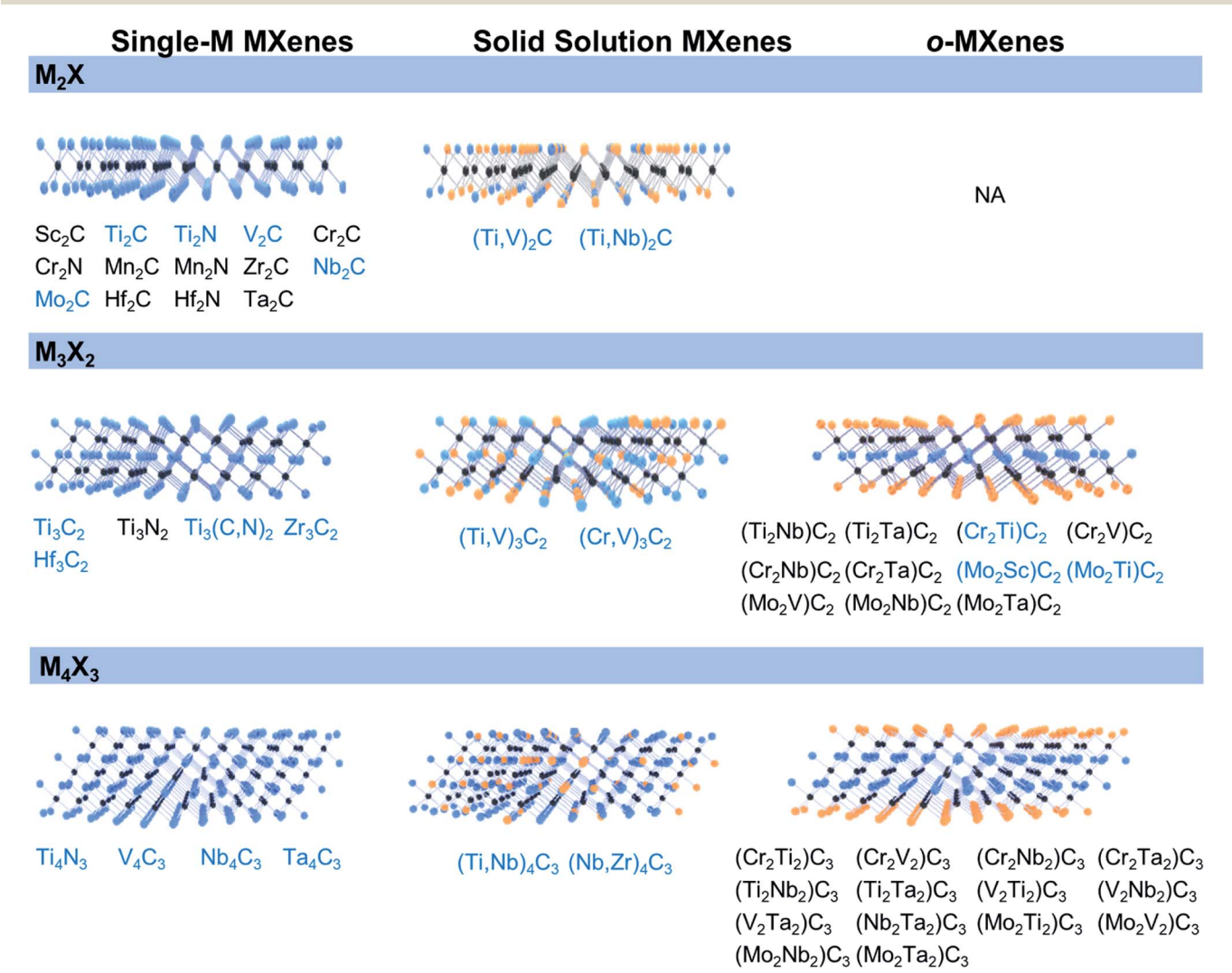

Fig. 3 The predicted (in black) and synthesized (in blue) MXenes classified by different types.

2.2 Synthesis of MXenes

MXenes are commonly synthesized by a top-down etching process in which "A" layers are selectively etched from their corresponding MAX phases.[17] The "M–A" metallic bonds are more active in contrast with covalent/ionic/metallic bonds between M and X.[13,59,60] Hydrofluoric acid (HF) was the first used etchant to synthesize MXenes (Fig. 4a).[61] In 2011, Gogotsi *et al.* found that the Al atomic layers in Ti_3AlC_2 can be selectively etched using 50% HF due to the high reactivity between the Al-containing MAX phase and F^-, resulting in accordion-like $Ti_3C_2T_x$ powder.[61] After the synthesis of $Ti_3C_2T_x$ by this method, many Al-containing MAX phases, *e.g.*, V_4AlC_3, V_2AlC, Mo_2TiAlC_2, Ta_4AlC_3, and Nb_2AlC, were etched with HF to produce the corresponding MXenes. However, HF is a type of toxic and hazardous reagent, which threatens the environment and the human body. Researchers are exploring milder and safer ways to synthesize MXenes.[1,62] One method is to produce HF *in situ*, and the typical reaction is that HF can be formed in the reaction between hydrochloric acid and metal fluorides such as LiF and KF.[63,64] Besides, HF can also be synthesized through the hydrothermal process of ammonium fluoride and hydrolysis of ammonium bifluoride solution (Fig. 4b).[65,66] After reacting with fluorine-containing compounds, the obtained MXenes are always decorated with many surface terminations such as –OH, –O, and/or –F.[67] By using this method, many carbide MXenes have been synthesized, such as $Ti_3C_2T_x$,[63] Nb_2CT_x,[64,68] and $Zr_3C_2T_x$.[69]

Additionally, using molten fluorides as etchants with the assistance of high temperature is an effective approach to acquiring MXenes, especially for those with high formation energy such as nitride MXenes.[70,75] For example, Gogotsi *et al.* first reported the synthetic process of 2D transition metal nitride (Ti_2N_3), in which a molten fluoride salt was used to etch Al from the Ti_4AlN_3 precursors at 550 °C under an argon atmosphere (Fig. 4c).[70] More recently, researchers paid more attention to fluorine-free ways to produce MXenes, including Lewis acid molten salt etching,[71,76,77] alkali etching,[72,78,79] and electrochemical etching.[80,81] Among them, Lewis acid molten salt etching is one of the most promising methods. Huang *et al.* designed a route in which the Zn element in molten $ZnCl_2$ replaced the Al element in MAX phase precursors, resulting in the synthesis of Ti_3ZnC_2, Ti_2ZnC, Ti_2ZnN, and V_2ZnC.[71] Surprisingly, when $ZnCl_2$ was excessively used in this fabrication route, Cl-terminated MXenes were obtained (Fig. 4d). Therefore, the Lewis acid molten salt etching route was also

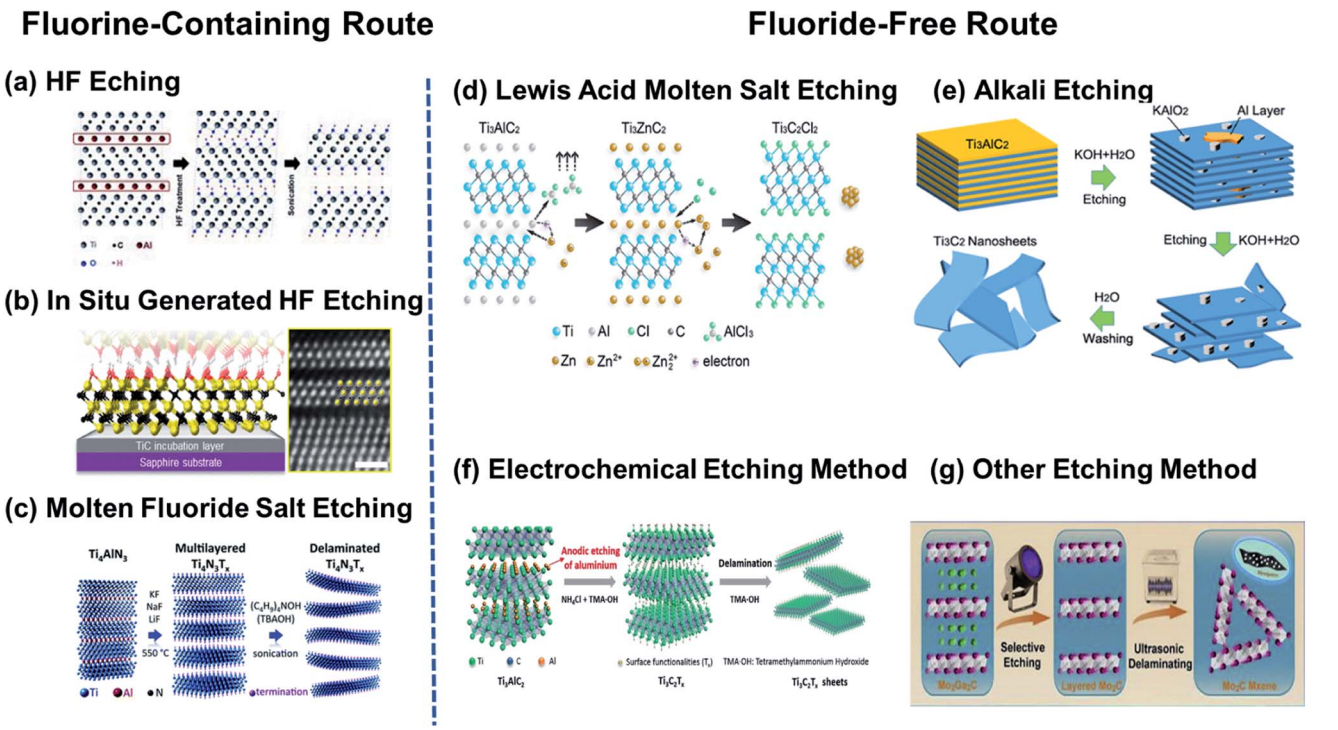

Fig. 4 Schematic diagram of the top-down selective etching method for preparing MXenes. (a) The exfoliation process of replacing an Al atom with –OH in the reaction of Ti_3AlC_2 and HF. Reproduced with permission.[61] Copyright 2011, Wiley-VCH. (b) The selective etching of OH-terminated Ti_3C_2 in ammonium bifluoride solution. Reproduced with permission.[66] Copyright 2014, American Chemical Society. (c) The synthesis of $Ti_4N_3T_x$ by molten fluoride salt treatment of Ti_4AlN_3 at 550 °C under Ar, followed by delamination of the multilayered MXene by tetraethyl ammonium hydroxide (TBAOH). Reproduced with permission.[70] Copyright 2016, Royal Society of Chemistry. (d) The element replacement reaction between the Lewis acid molten salt ($ZnCl_2$) and MAX phase to produce Cl-terminated MXenes. Reproduced with permission.[71] Copyright 2019, American Chemical Society. (e) The synthesis of Cl-terminated MXenes by etching Ti_3AlC_2 precursors using KOH solution. Reproduced with permission.[72] Copyright 2017, American Chemical Society. (f) Etching method based on the Ti_3AlC_2 anode and binary aqueous electrolyte. Reproduced with permission.[73] Copyright 2018, Wiley-VCH. (g) UV-induced selective etching route of removing the double Ga layers from Mo_2Ga_2C precursors to generate Mo_2C. Reproduced with permission.[74] Copyright 2020, Elsevier.

used to modify the surface termination and etch non-Al MAX phases.[76,77] An alkali is also a kind of feasible etchant owning to the strong binding ability between hydroxyl from the etching solution and the amphoteric element Al of MAX.[67,78] Xie *et al.* put forward a two-step etching process in which Ti_3AlC_2 was first soaked in NaOH solution, and then hydrothermally treated using H_2SO_4 to obtain $Ti_3C_2T_x$.[82] In this process, NaOH was used to leach the Al layer selectively, and H_2SO_4 helped to remove surface-exposed Al. Li *et al.* successfully fabricated single-layered $Ti_3C_2(OH)_2$ nanosheets by etching Ti_3AlC_2 precursors with KOH in the presence of a small amount of water (as shown in Fig. 4e).[72] However, alkali etching synthesis methods are still facing some difficulties like complex separation operations, high alkali concentration, and strict temperature requirements, thereby leading to a low MXene yield.[79]

As for the electrochemical etching method, Al atomic layers can be selectively removed under a certain voltage using MAX phases as the electrode with NaCl, HCl, or HF as the electrolytic solution.[67,83] The advantage of this approach lies in that the structure of MXenes can be precisely controlled by accurately managing the etching voltage window in the range of reaction potentials between A and M layers as well as regulating the appropriate etching time.[67,84] However, it is unavoidable that the parent MAX phases are often over etched and generate concomitant products, *i.e.* carbide-derived carbon (CDC),[81] which decreases the yield of MXenes. Therefore, many researchers made efforts to overcome this drawback.[80] For instance, Yang *et al.* demonstrated an efficient etching method based on a Ti_3AlC_2 anode and binary aqueous electrolyte (Fig. 4f).[73] To ensure a continuous etching process and avoid the production of CDC, some intercalators such as TMAOH were used to enhance the accessibility of electrolyte ions into the Al layer. In addition to the etching methods mentioned above, recently, other methods like using a halogen as an etchant[85] or applying mechanical and electromagnetic waves to assist etching have also been reported. For example, Mei *et al.* proposed an effective UV-induced selective etching method without fluorine involved to fabricate mesoporous Mo_2C MXene from Mo_2Ga_2C (Fig. 4g).[67,74]

After etching, stacked multi-layer MXenes, connected by van der Waals forces and hydrogen bonding, are usually obtained, which have fewer advantages compared to mono-layered MXenes.[12] Therefore, delamination is necessary to get single layers with high surface space, good hydrophilicity, and rich surficial functional groups.[86,87] A mechanical process like ultrasonic treatment was firstly used (Fig. 4a and g), while generally low yields were achieved due to the inability to disrupt strong interlaminar interactions. When metal halides such as LiF and KF were used in the preparation of MXenes, it has been found that metal ions can enter the space between the layers, leading to the increase of the layer space.[63] In this case, metal halides are excellent inorganic intercalators, allowing etching and exfoliation to occur simultaneously. Up to now, new organic intercalators, including dimethyl sulfoxide (DMSO),[88] TBAOH (Fig. 4c),[89] and tetramethylammonium hydroxide (TMAOH) (Fig. 4f),[90] have been developed to meet the demand for more efficient delaminating.[86]

3. MXenes as catalysts

MXenes are an emerging group of materials in the field of thermal catalysis (Table 1). Due to the high thermal stability[91,92] and unique structures,[44] MXenes show some advantages compared with traditional catalysts. Among the numerous kinds of MXenes, $Ti_3(C/N)_2T_x$, Mo_2CT_x, and V_2CT_x have been intensively studied because of the relatively mature preparation process and the easy modification of their structures. Therefore, in this section, we describe the thermal catalytic reactions that occur on the above-mentioned MXenes ($Ti_3(C/N)_2T_x$, Mo_2CT_x, and V_2CT_x) as shown in Fig. 5, and compare MXenes with other catalysts from structures to activities. Furthermore, we summarize the specific roles of surface termination groups and propose the active sites on MXenes in the thermal catalytic reactions.

3.1 $Ti_3(C/N)_2T_x$

$Ti_3C_2T_x$ is the first synthesized and the most-commonly used MXene material. Compared with other metal-based catalysts,

Table 1 The catalytic performance of MXenes

Catalyst	Reaction	Main reactant	T (°C)	P (MPa)	Conv.[a] (%)	Target product	Selec.[b] (%)	Ref.
$Ti_3C_2T_x$	Furfural hydrogenation	Furfural	180	5.0	36	Furfuryl alcohol	52	93
Ti_3CNT_x	Furfural hydrogenation	Furfural	180	5.0	46	Furfuryl alcohol	49	93
$Ti_3C_2T_x$	Guaiacol hydrodeoxygenation	Guaiacol	350	5.0	56	Phenol	61	94
$Ti_3C_2T_x$	Ethylbenzene dehydrogenation	Ethylbenzene	550	0.1	21	Styrene	97.5	95
$Ti_3C_2T_x$	HCOOH dehydrogenation	HCOOH	80	0.1	94	H_2	100	41
Ti_3C_2	DBT[c] oxidative desulfurization	DBT[c]	130	0.1	95.7	$DBTO_2$[d]	—	96
Ti_3C_2/Ti_3AlC_2	DBT[c] oxidative desulfurization	DBT[c]	130	0.1	99.0	$DBTO_2$[d]	—	44
2D-Mo_2C	CO_2 hydrogenation	CO_2	430	2.5	38	CO	94	51
V_2CT_x	CH_4 dehydroaromatization	CH_4	700	0.1	11.8	C_6H_6	4.84	97
2D-Mo_2CO_x/SiO_2	CH_4 dry reforming	CH_4	800	1.0	80	CO, H_2	CO : $H_2 \sim 1.5$	98
Multilayered-V_2CT	CH_4 dry reforming	CH_4	800	0.1	78	CO, H_2	CO : $H_2 \sim 0.9$	99
Mo_2CT_x	Water–gas shift reaction	CO	500	0.1	18	CO_2, H_2	>99	100

[a] Conversion refers to the conversion of the main reactant. [b] Selectivity refers to the selectivity of the target product. [c] DBT is dibenzothiophene. [d] $DBTO_2$ is dibenzothiophene sulfone.

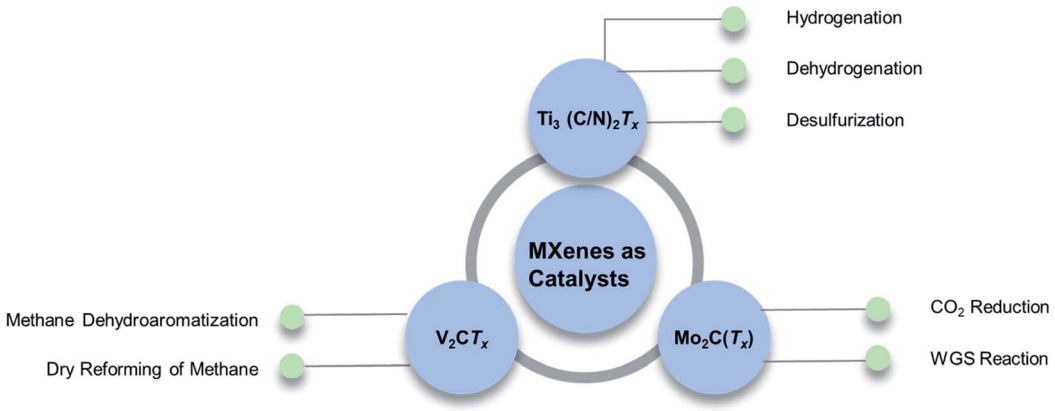

Fig. 5 Commonly used MXene species as catalysts and their applications in thermal catalysis.

$Ti_3(C/N)_2T_x$ features strong thermal stability, which is ascribed to the $M_{n+1}X_n$ skeleton formed by carbonic atomic (C) layers and transition metal (Ti) atomic layers.[101] Besides, the surface terminations generated during the synthetic process contribute a variety of properties such as hydrophilicity and highly diffusing Lewis acidity to $Ti_3(C/N)_2T_x$.[102] Therefore, $Ti_3(C/N)_2T_x$ shows promising catalytic performance in hydrogenation,[93,94] dehydrogenation,[41,95] and desulfurization reactions of complex organic compounds, such as biomass and polycyclic organics. In this part, we analyze the role of the unique structure of $Ti_3(C/N)_2T_x$ in improving the activity of hydrogenation, dehydrogenation, and other reactions. Moreover, the influence of termination groups and carbide-metal-termination bonds of $Ti_3(C/N)_2T_x$ on the catalytic reactions is discussed.

3.1.1 Hydrogenation. Hydrogenation is the key step in upgrading various lignocellulosic platform chemicals like levulinic acid, furfural, phenols, and guaiacol.[103,104] However, it is still challenging to control the product selectivity in the hydrogenation of biomass-derived compounds, because these reaction pathways are quite complex and accompanied by various side reactions.[104] Naguib *et al.* first applied Ti-based MXenes as catalysts to selectively hydrogenate furfural (a substance derived from hemicelluloses).[93] Under the catalysis of $Ti_3C_2T_x$ with H_2 as the reducing agent, the main product, furfuryl alcohol, was produced at a rate of 145 $mmol_{furfural}$ g^{-1} h^{-1} and a selectivity of 52%, which was higher than that of TiO_2-based materials (rutile, anatase, and P25) under the same conditions. The reason was that the metal–oxygen site pair of MXenes played an important role. On this peculiar pair of MXenes, heterolytic activation of hydrogen occurred, and then the selective hydrogenation of the carbonyl bond proceeded *via* the addition reaction of the proton and hydride to the C and O atoms. Moreover, the Ti_3CNT_x catalyst showed similar activity (126 $mmol_{furfural}$ g^{-1} h^{-1}) and selectivity (49%) for furfuryl alcohol, but higher stability compared with $Ti_3C_2T_x$. The better performance of Ti_3CNT_x against deactivation was ascribed to the lower coverage reaction products caused by less diverse termination groups on its surface, indicated by a single Ti_3CNT_x (0002) peak at around 8° in XRD corresponding to a *c* lattice parameter (*c*-LP) of 21.9 Å (Fig. 6a). In contrast, the deactivation of $Ti_3C_2T_x$ came from multiple intercalation states due to the reaction occurring on the surface termination groups of MXenes, which was proved by the replacement of the (0002) peak in pristine $Ti_3C_2T_x$ (2θ of 8.96°) by three new peaks (3.94°, 5.56°, and 9.24°), as shown in Fig. 6b.[93]

Besides hydrogenation, upgrading biomass-derived compounds by removing the oxygen groups is equally desirable. A $Ti_3C_2T_x$ nano-sheet was a type of unique catalyst with superior performance in hydrodeoxygenation (HDO).[94] With this catalyst, guaiacol, a lignin-derived compound, was converted to phenol and methylanisole at a selectivity of 61% and 17%, respectively, at 350 °C and 5.0 MPa. Furthermore, $Ti_3C_2T_x$ served as a bifunctional catalyst simultaneously promoting the demethylation (DME) reaction of anisole to produce phenol (Fig. 6c). In this process, the main products were phenol and methylanisole with similar selectivities of 45% and 38%, respectively. In comparison with metal carbide (Re, Ru, Ni, Fe, and Cu) catalysts, the phenol selectivity of $Ti_3C_2T_x$ was the highest, which can be ascribed to the surface termination groups of MXenes.[105] To be specific, the surface termination groups contained weak basic sites and acid sites. The acid sites were derived from the F termination and Ti element, on which methylanisole has been obtained by bi-molecular transalkylation. The C–Ti–O structure provided basic sites, where the direct demethoxylation (DMO) of guaiacol was expected to occur.

3.1.2 Dehydrogenation. Dehydrogenation plays an important role in the refinery cracking process where saturated alkanes are turned into olefins and aromatic compounds.[106,107] However, during this process, a high selectivity and yield only can be obtained at high temperatures (~620 °C); hence, excess steam must be provided simultaneously to alleviate catalyst coking.[106,107] To surmount this obstacle, carbon-based catalysts, like graphene and carbon nanotubes, were applied, and $Ti_3C_2T_x$ was also explored to catalyze the direct dehydrogenation reaction of ethylbenzene (EB).[106] In this routine, by using $Ti_3C_2T_x$ as the catalyst, styrene (ST), an important and greatly demanded industrial monomer, was obtained with a high reactivity of 92 μmol m^{-2} h^{-1} and a high selectivity of 97.5% at a relatively low temperature (550 °C). In contrast, the reactivity of the analogous

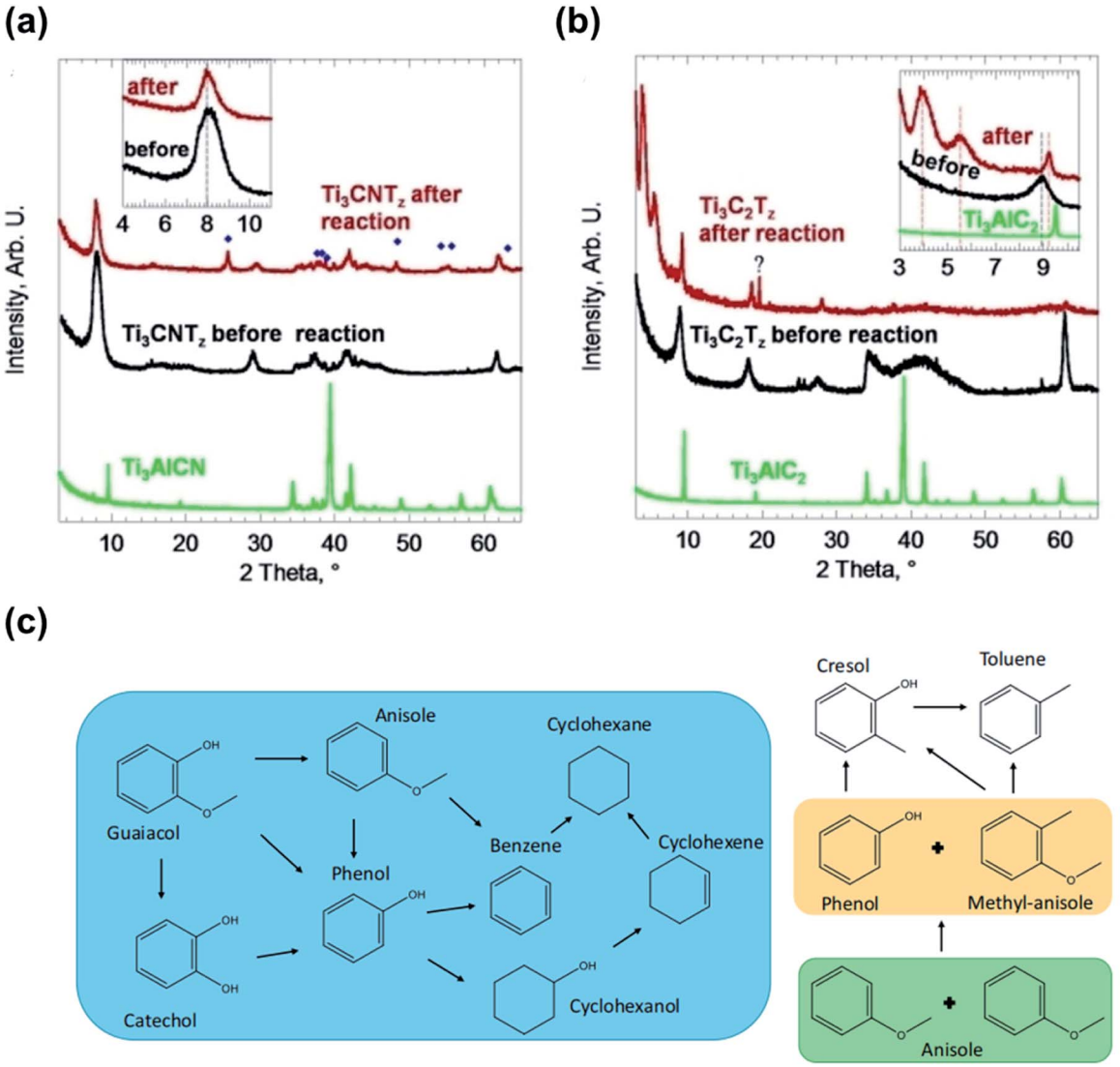

Fig. 6 The applications of $Ti_3C_2T_x$ in hydrogenation. (a) Ti_3CNT_x before and after hydrogenation. (b) $Ti_3C_2T_x$ before and after hydrogenation. The (0002) peak areas are presented in the insets, and the blue diamonds represent the peak position of anatase [PDF# 02-0406]. Reproduced with permission.[93] Copyright 2020, Wiley-VCH. (c) The conversion mechanism of guaiacol, anisole, and phenol. Reproduced with permission.[94] Copyright 2020, Elsevier.

graphene, nanodiamond, and TiC-derived carbon (TiC-CDC) was 12, 7, and 0.87 μmol m^{-2} h^{-1} respectively, much lower than that of $Ti_3C_2T_x$ (Fig. 7a). The reason why the MXenes boosted the dehydrogenation reaction could be ascribed to the C–Ti–O bonds, the most abundant types among multiple chemical environments of O elements (Ti–O, C–Ti–O, C–Ti–OH, and Al–O). On C–Ti–O bonds, the energy barrier of the dehydrogenation process was significantly reduced. According to first-principles calculations, the first C–H bond of EB was activated with an energy barrier of 0.66 eV, and the second hydrogen abstraction barrier was 0.46 eV. Moreover, $Ti_3C_2T_x$ can catalyze the EB conversion at a stable rate for *ca.* 40 h without obvious deactivation (Fig. 7b). In contrast, commercial iron oxide suffered from significant coke deposition for the same period.

Recently, the hydrogen-release reaction is another dehydrogenation reaction that has attracted emerging attention.[108] Hou *et al.* prepared rich oxygen-covered $Ti_3C_2T_x$ to boost the catalytic activity of HCOOH dehydrogenation.[41] In this reaction, HCOOH was finally converted into CO_2 with the liberation of hydrogen at a space-time-yield (STY) of 365 $mmol^{-1}$ g^{-1} h^{-1} and 100% selectivity. According to DFT calculations, the rich-oxygen-covered surface of $Ti_3C_2T_x$ acted as the active site. On these sites, HCOOH was adsorbed with an adsorption energy of −3.05 eV, followed by spontaneous dissociation to generate HCOO* and H* with an energy barrier (E_a) of only 0.25 eV. Then the dissociation of HCOO* occurred over $Ti_3C_2T_x$ with an E_a of only 0.61 eV, and CO_2 and H_2 were desorbed from $Ti_3C_2T_x$ with the energies of −0.16 and −0.06 eV, respectively. In a word, the remarkable catalytic performance of $Ti_3C_2T_x$ was due to the low

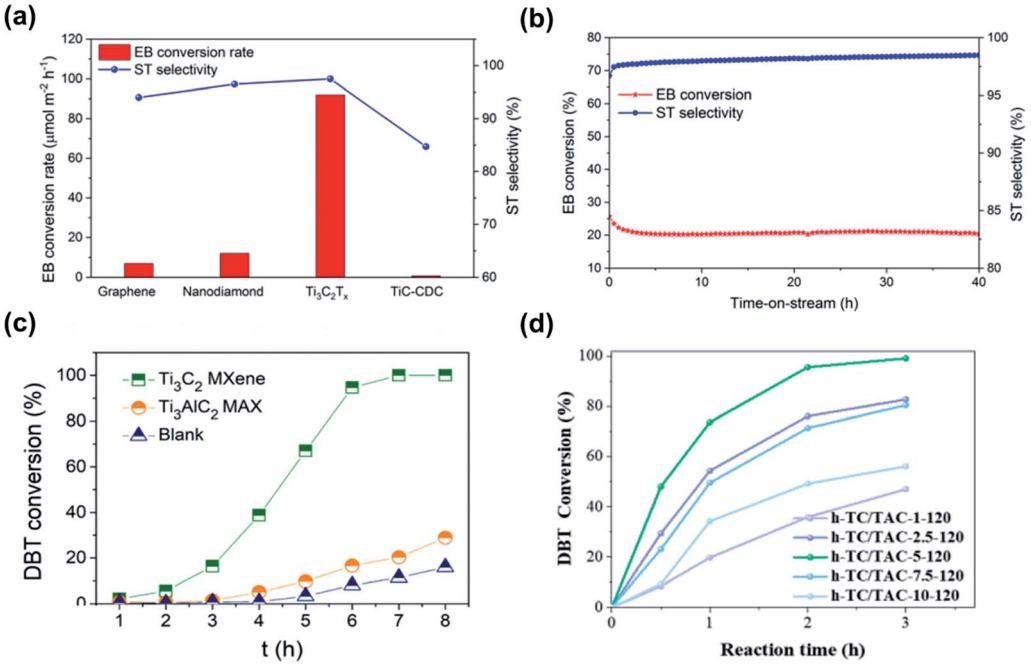

Fig. 7 The dehydrogenation and desulfurization reactions with $Ti_3C_2T_x$. (a) Ethylbenzene dehydrogenation reactivity with $Ti_3C_2T_x$ MXene, nanodiamond, graphene, and TiC-derived carbon (TiC-CDC). (b) Long-term stability of $Ti_3C_2T_x$ MXene in the dehydrogenation of ethylbenzene. Reproduced with permission.[95] Copyright 2018, American Chemical Society. (c) DBT conversion with different catalysts. Reproduced with permission.[96] Copyright 2021, Elsevier. (d) DBT conversion rates with h-TC/TAC-*x*-*y* prepared at different alkali concentrations and etching temperatures, where *x* is the concentration of the KOH etchant, and *y* is the etching temperature. Reproduced with permission.[44] Copyright 2022, Elsevier.

reaction energy barrier of the HCOO*-to-CO_2* step and low desorption energies of CO_2 and H_2.

3.1.3 Desulfurization. Oxidative desulfurization (ODS) is important to reduce SO_x emissions from petroleum fuel combustion processes,[109] but it often has low conversion and requires harsh conditions.[110] Transition metal carbides (W, Mo, V, Zr, and Ti) are commonly used as the catalysts for this reaction. For example, Ti_3C_2 was adopted to remove dibenzothiophene (DBT) and its derivative sulfides.[96] With a catalyst concentration of only 0.25 mg mL^{-1}, the DBT conversion reached 95.7% (Fig. 7c). By contrast, the conversion with TiO_2/graphite was merely 5.6%, and that with the MAX phase Ti_3AlC_2 was only 17.2%. Furthermore, when Ti_3C_2 was employed for the conversion of real diesel, the total sulfur concentration could be reduced from 186 to 24 ppm, and the total sulfur removal reached 87%. This was because the coordinated unsaturated metal Ti sites in the Ti_3C_2 MXene were easily oxidized by molecular oxygen to form TiO_2 clusters. The defective TiO_2 clusters generated dynamically on the surface of MXenes were highly active reaction sites where O_2 was converted into O_2^{2-} and $^{\bullet}O_2^{-}$, and further converted into RC(OOO)$^{\bullet}$ and $^{\bullet}$OH radicals.

Additionally, a kind of hydroxylated Ti_3C_2/Ti_3AlC_2 (h-TC/TAC) catalyst was prepared for the aerobic desulfurization of DBT.[44] The h-TC/TAC prepared in a 5 mol L^{-1} KOH etchant at 120 °C for 24 h exhibited a desulfurization rate of up to 99% (Fig. 7d) and can be recycled eight times without significant deactivation. In this reaction, the oxygen species on the catalyst surface including Ti–O and Ti–OH could be considered as possible active species for ODS, on which the molecular oxygen was converted into $^{\bullet}$OH and $^{\bullet}O_2^{-}$ continuously. Therefore, DBT can be easily absorbed on the surface of the catalysts and further oxidized by these two radicals.

3.2 $Mo_2C(T_x)$

3D molybdenum carbide Mo_2C has been widely applied in CO_2 reduction,[111–114] propane activation,[115] and HDO reactions, due to its platinum-like catalytic performance.[39,40,116,117] More recently, 2D molybdenum carbide (2D-Mo_2C or Mo_2CT_x), has shown promising performance in CO_2 reduction[51,98] and the water-gas shift (WGS) reaction.[100] In this part, we summarize the effect of the pores in layered structures on accelerating the adsorption process and try to clarify the effect of surface termination groups on catalyst activity and stability.

3.2.1 CO_2 reduction (dry reforming and CO_2 hydrogenation). The reduction of CO_2 to valuable chemicals and fuels to mitigate the greenhouse effect has received wide attention.[118,119] However, there are two major obstacles that limit its development, *i.e.*, the CO_2 adsorption energy barrier[120,121] and difficulties in precisely controlling the selectivity of products.[122] Recently, $Mo_2C(T_x)$ was applied in the CO_2 reduction reaction as a new type of catalyst.[51] For instance, a multilayered hexagonal 2D-Mo_2C material with only Mo-terminated basal planes was synthesized by treating Mo_2CT_x at 500 °C for 2 h under 100% H_2. This material featured high selectivity and activity in reverse water–gas shift (RWGS). To be precise, under the catalysis of 2D-Mo_2C, the formation rate of CO reached 475 mg h^{-1} g_{cat}^{-1}, and

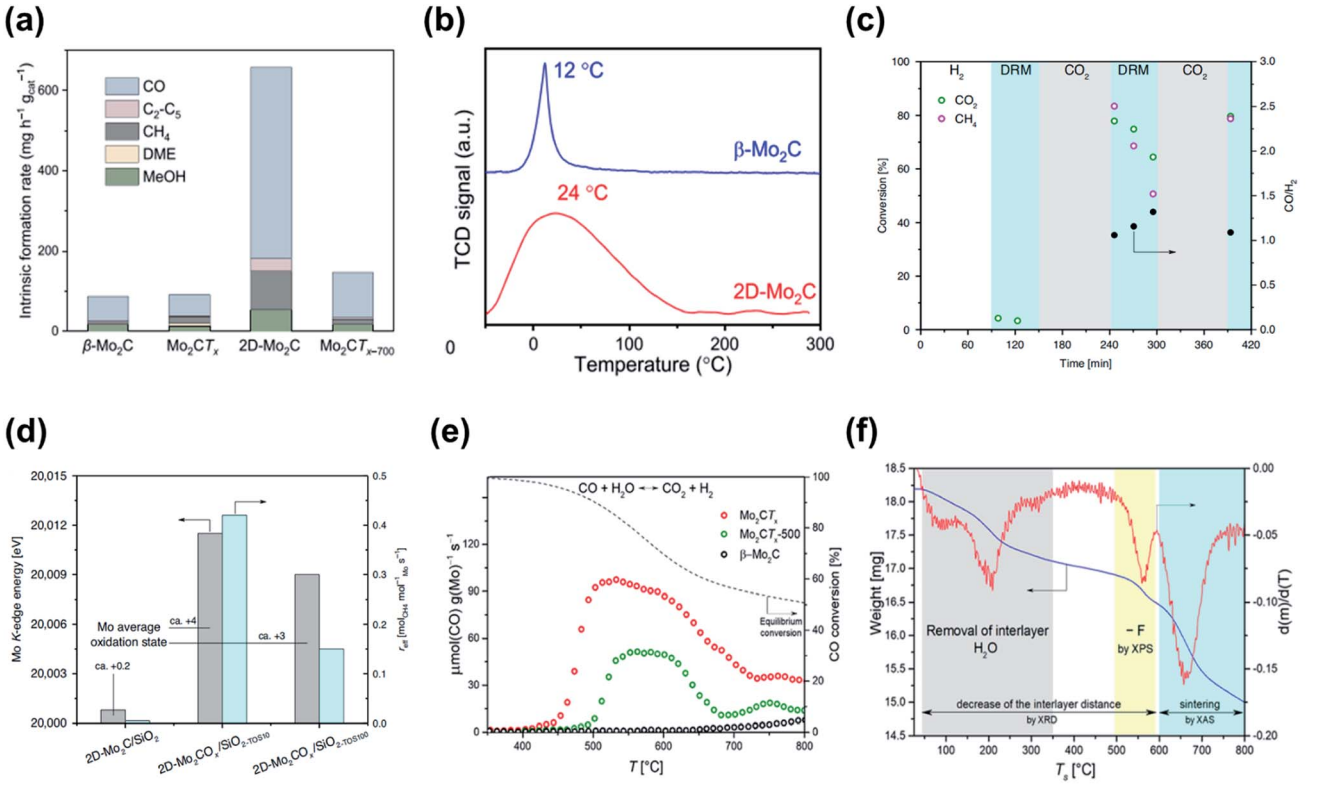

Fig. 8 The thermal catalysis with Mo_2CT_x. (a) Intrinsic formation rates of β-Mo_2C, Mo_2CT_x, 2D-Mo_2C, and $Mo_2CT_{x\text{-}700}$. (b) CO temperature-programmed desorption (TPD) of 2D-Mo_2C and β-Mo_2C. Reproduced with permission.[51] Copyright 2021, Springer Nature. (c) Catalytic performance of 2D-Mo_2C/SiO_2 (90–150 min) and 2D-Mo_2CO_x/SiO_2 (240–300 min and from 390 min after the CO_2 regeneration step) in DRM. (d) Correlation of the Mo oxidation state (determined by Mo K-edge XANES), and the catalytic activity of 2D-Mo_2C/SiO_2, 2D-$Mo_2CO_x/SiO_{2\text{-TOS10}}$, and 2D-$Mo_2C/SiO_{2\text{-TOS100}}$. Reproduced with permission.[98] Copyright 2020, Springer Nature. (e) WGS catalytic activity of Mo_2CT_x, $Mo_2CT_{x\text{-}500}$, and a reference β-Mo_2C. (f) *In situ* structural stability of Mo_2CT_x studied by TGA H_2-TPR. Reproduced with permission.[100] Copyright 2019, American Chemical Society.

the selectivity of CO was 94%. However, the CO formation rates with β-Mo_2C and Mo_2CT_{x-700}, which sintered into the 3D structure, are only 17% and 33% of that with 2D-Mo_2C, respectively (Fig. 8a). According to CO temperature-programmed desorption (TPD) experiments, on the one hand, this high catalytic activity stemmed from mass transfer effects. In 2D-Mo_2C, reactive gas can be adsorbed both on the surface and inside the 2D pores of this multilayered material, indicated by a broad CO desorption peak at 24 °C (Fig. 8b). However, the adsorption only occurred on the surface of β-Mo_2C and Mo_2CT_{x-700} due to their bulk structures. On the other hand, the high activity was attributed to the high exposure of Mo sites on 2D-Mo_2C without the blocking of the termination groups ($-T_x$).

Moreover, two-dimensional molybdenum oxycarbide supported on silica (2D-Mo_2CO_x/SiO_2) was found to have great activity and selectivity for the dry reforming of methane (DRM).[98] The synthesis of 2D-Mo_2CO_x/SiO_2 was divided into two steps. The first step was treating 2D-Mo_2CT_x/SiO_2 under H_2 (750 °C, 0.5 h) to prepare 2D-Mo_2C/SiO_2, and the second step was exposing 2D-Mo_2CT_x/SiO_2 to a CO_2 atmosphere to prepare 2D-Mo_2CO_x/SiO_2. Compared with 2D-Mo_2C/SiO_2 showing negligible DRM activity, 2D-Mo_2CO_x/SiO_2 was highly active with a methane conversion rate of 0.42 $mol_{(CH_4)}$ $mol_{(Mo)}^{-1}$ s^{-1} after a time on stream (TOS) of 10 min at 80% CH_4 conversion (Fig. 8c). The improved catalytic activity of 2D-Mo_2CO_x/SiO_2 can be attributed to the suitable oxidation state of Mo in the 2D-nanosheet catalyst. XANES indicated that if the oxidation of 2D-Mo_2C/SiO_2 was carried out under DRM conditions (730 °C, $CH_4 : CO_2 = 1 : 1$, space velocity (SV) $= 3 \times 10^4$ L g_{Mo}^{-1} h^{-1}, and contact time of 0.1 ms g_{Mo} mL^{-1}) for a TOS of 10 min (2D-$Mo_2COh_x/SiO_{2\text{-TOS10}}$), the Mo oxidation state of 2D-Mo_2CO_x/SiO_2 was +4, which was highly active in DRM (Fig. 8d). However, if the oxidation of 2D-Mo_2C/SiO_2 was conducted at 800 °C in a CO_2 atmosphere, the surface of 2D-Mo_2CO_x/SiO_2 was covered by oxygen and the average Mo oxidation state was +5.5, which was inactive for DRM. Moreover, DFT calculations further explained why the exact oxidation state resulted in the higher activity, *i.e.*, the suitable oxygen coverage played a significant role in reducing the binding energy of C* and O* species and lowered the energy barriers of the C–O coupling in the CH_4 cleavage process, which was the rate-limiting step in DRM.

3.2.2 Water–gas shift reaction. The water–gas shift (WGS) reaction is a significant step in many industrial processes, including ammonia synthesis, methanol synthesis, and hydrogen production. However, the current industrial catalysts

are unstable and normally require lengthy activation steps.[123–125] In a recent study, Mo_2CT_x was applied in WGS with high activity and stability.[100] At around 520 °C, Mo_2CT_x reached the maximal activity with a CO consumption rate of *ca.* 100 $\mu mol_{(CO)}\ g_{(Mo)}^{-1}\ s^{-1}$ and a selectivity of 99%. However, under similar conditions, the activity of Mo_2CT_x-500 (reducing Mo_2CT_x at 500 °C in 20% H_2/N_2) was much lower than that of Mo_2CT_x, and the reference material β-Mo_2C was completely inactive for this reaction (Fig. 8e). This phenomenon was attributed to the mass transfer limitation. In Mo_2CT_x-500, its interlayer distance decreased, which resulted in the reduction of reactant transfer capacity. Meanwhile in β-Mo_2C, the mass transport process was hindered by its bulk structure. In the H_2 TPR study, only interlayer water was desorbed from Mo_2CT_x below 350 °C, and it did not undergo any structural change. When the temperature reached 500 °C, the interlayer spacing of Mo_2CT_x decreased obviously due to the violent de-functionalization and the removal of the intercalated water, but it can still maintain the integrity of the structure. When the temperature reached 600 °C, two-dimensional Mo_2CT_x sheets started sintering to a bulk carbide phase (Fig. 8f).

3.3 V_2CT_x-derived catalysts

V_2CT_x is another commonly reported and used MXene material after Ti_3CT_x. Thakur *et al.* employed V_2CT_x in methane dehydroaromatization (MDA) to directly convert methane (CH_4) into benzene (C_6H_6) at 700 °C.[99] The catalyst showed a state-of-the-art CH_4 conversion of 11.8% with a C_6H_6 formation rate of 1.9 mmol $g_{cat}^{-1}\ h^{-1}$ at 700 °C (Fig. 9a). Conversely, V_2AlC exhibited no reactivity in the MDA reaction. The good performance, on the one hand, was attributed to the interlamellar space, which provided the confinement for the oligomerization and cyclization of intermediates (C2 species) to then form benzene. On the other hand, the Lewis and Brønsted sites originating from surface termination groups made a significant contribution to the oligomerization reaction of $*C_2H_3$ (intermediates of MDA) to form benzene (Fig. 9b). However, at this temperature, the MXene structure was converted into amorphous non-MXene phases. Moreover, after the long-term reaction, some solid amorphous and graphitic carbon grew on the surface of V_2CT_x dervied catalysts. (a) CH4 conversion and (Fig. 9c), limiting the accessibility of CH_4 inside the channels, resulting in the deactivation of this catalyst.

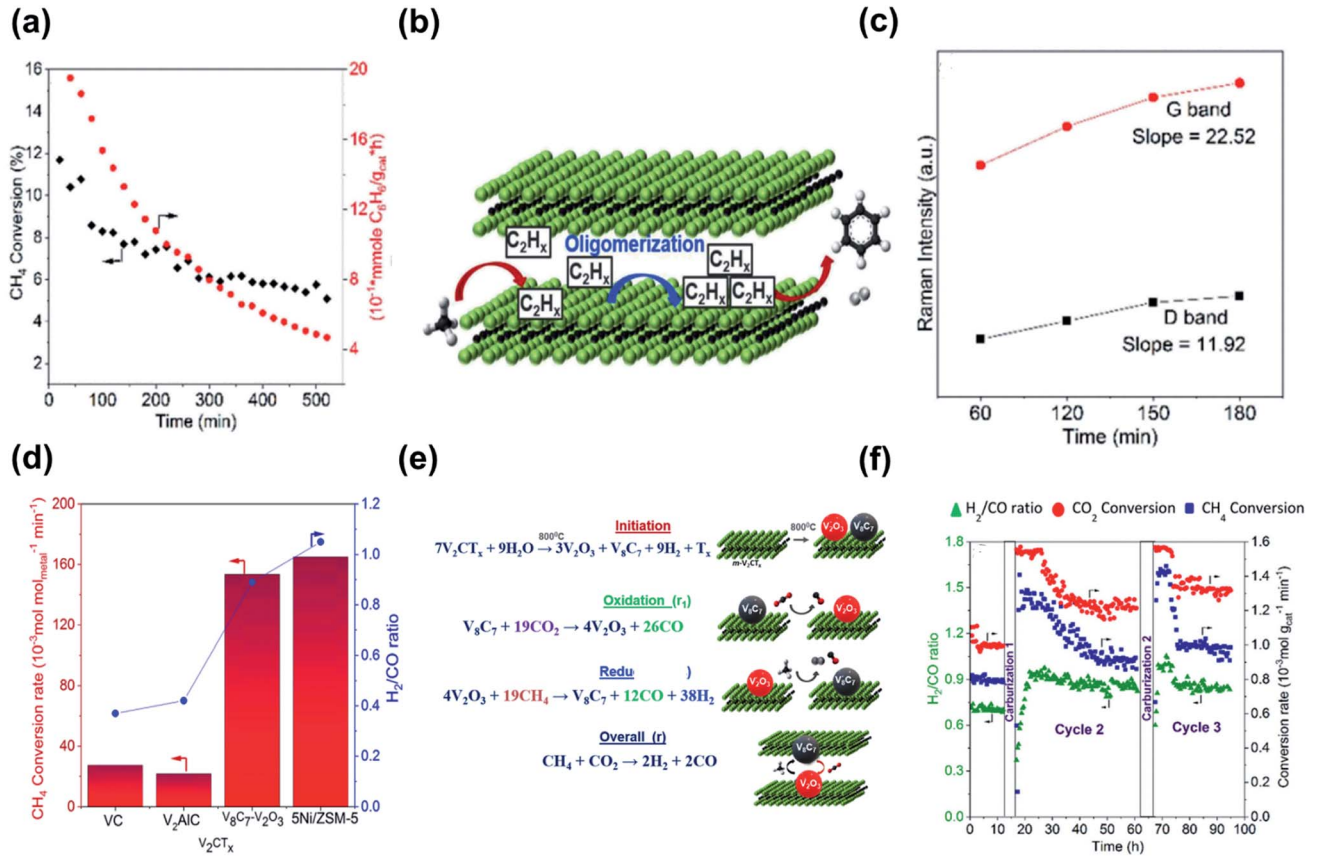

Fig. 9 The thermal catalysis with V_2CT_x-dervied catalysts. (a) CH_4 conversion and C_6H_6 formation rates with V_2CT_x. (b) Schematic illustration of forming C_6H_6 on V_2CT_x-dervied catalysts. (c) The relationship between the relative formation rate of D (1351 cm^{-1}) and G (1592 cm^{-1}) bands and TOS. Reproduced with permission.[99] Copyright 2020, Wiley-VCH. (d) CH_4 conversion and H_2/CO ratio with VC, V_2AlC, V_2O_3–V_8C_7/m-V_2CT_x MXene, and 5Ni/ZSM-5. (e) Proposed DRM mechanism using the m-V_2CT_x MXene-derived catalyst. (f) CH_4 and CO_2 conversion activity and H_2/CO ratio with V_2O_3–V_8C_7/m-V_2CT_x of surface termination groups for 96 h. Reproduced with permission.[97] Copyright 2020, American Chemical Society.

Moreover, multilayered vanadium carbide (m-V_2CT_x) can also serve as the precursor for a robust oxy-carbide catalyst in DRM.[97] This material showed an attractive activity in DRM, converting about 78% of CH_4 with a rate of 153.4 $mmol_{CH_4}$ mol_V^{-1} min^{-1}, which was comparable to the CH_4 conversion rate of Ni-based catalysts and was about four times higher than that of its bulk counterparts V_2AlC MAX phase and commercial VC (Fig. 9d). In this DRM process, V_2O_3 and V_8C_7 nanocrystals were generated *in situ* both on the surface and layered structure of V_2CT_x, resulting in maximizing the utilization of active and selective V sites on the new V_2O–V_8C_7/m-V_2CT_x. The detailed process was revealed by isotopic labeling experiments with $^{13}CO_2$ and $^{13}CH_4$. Initially, when heated to 800 °C under an inert gas, m-V_2CT_x was partially oxidized to V_2O_3, while some of the MXene transformed into V_8C_7 particles. V_8C_7/m-V_2CT_x was oxidized by CO_2 to form V_2O_3/m-V_2CT_x and CO. Meanwhile, recarburization of V_2O_3/m-V_2CT_x with CH_4 resulted in the formation of V_8C_7/m-V_2CT_x CO and H_2 (Fig. 9e). Therefore, the competition between the oxidation reaction and the carburization reaction resulted in a more stable material with the CH_4 and CO_2 conversion rates of 1.0 $mmol_{(CH_4)}$ g_{cat}^{-1} min^{-1} and 1.3 $mmol_{(CO_2)}$ g_{cat}^{-1} min^{-1} respectively even after 96 h on stream (Fig. 9f).[97]

3.4 Influence of surface terminations

Many significant properties of MXenes such as hydrophilicity, conductivity,[58] and stability can be tuned by controlling the number and variety of surface termination groups T_x. Similarly, the activity and selectivity of MXenes in thermal catalytic reactions can also be affected by changing T_x groups. This is attributed to the influence of T_x groups on adjacent transition metal atoms and surface properties. Therefore, in this part, we sum up the methods to vary the types and coverage of the surface termination groups and further summarize the role of T_x from three aspects: (i) influencing the exposure of the transition metals, (ii) affecting the oxidation states of the adjacent transition metal atoms, and (iii) altering the acid–base properties (Fig. 10).

The variation of surface terminations can be realized by heat treatment, in which the temperature and atmosphere are two significant factors. Under a reductive environment, surface termination groups are removed. In dilute H_2, only partial T_x groups can be removed from Mo_2CT_x even when the temperature rose to 500 °C.[51] Specifically, when 5% H_2/Ar acted as the reducing gas, hydroxyl and part of fluorine were reduced from the Mo_2CT_x surface at 280 °C, and subsequently, oxo groups and most of the fluorine were removed at 500 °C. However, if pure H_2 was used, the removal of partial T_x occurred at a relatively lower temperature at 175 °C, while at 500 °C all the surface termination groups were totally defunctionalized from the Mo_2CT_x surface. The hydrogen treatment process of V_2CT_x was also investigated, in which the removal of T_x groups occurred above 300 °C, and VO_x species on its surface were reduced simultaneously.[126] Furthermore, the termination variation of

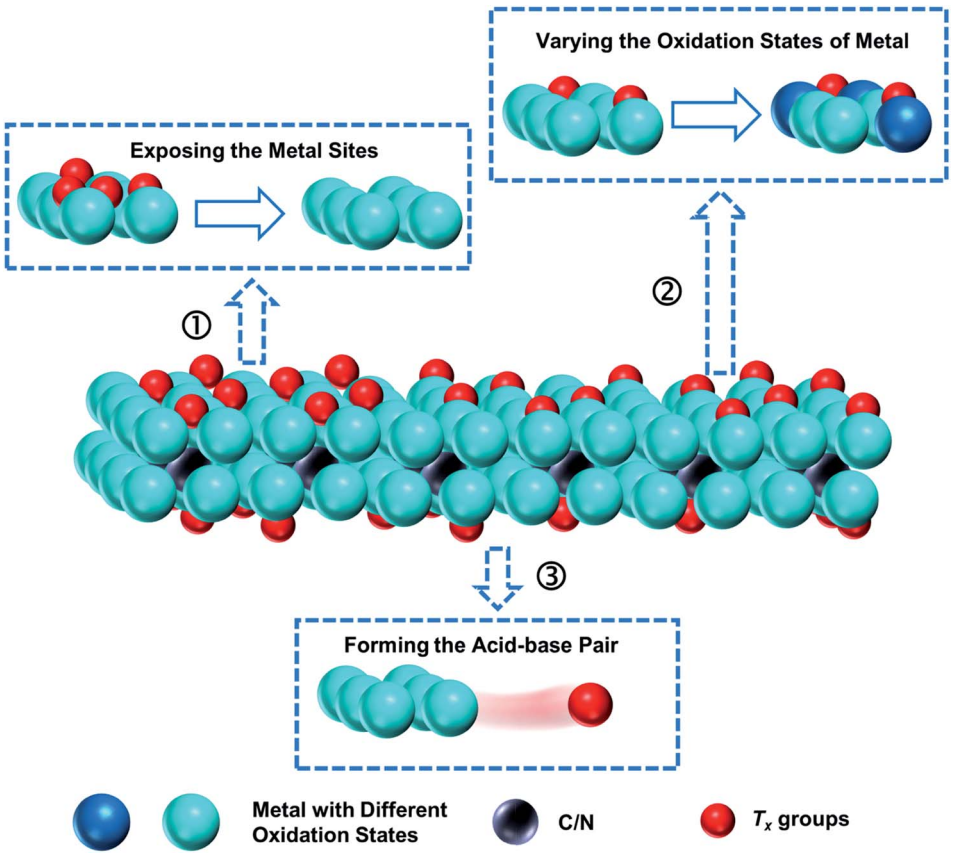

Fig. 10 Schematic diagram of the influence of surface termination groups.

V_2CT_x in inert and oxidative environments was also researched. The result was that N_2-treated V_2CT_x was extremely stable even up to 600 °C, and only minor oxidation occurred on its surface. Under CO_2, the material was oxidized above 300 °C, leading to the surface covering a larger percentage of VO_x species.

More transition metal atoms will be exposed as T_x groups are removed. In the comparison of Mo_2CT_x and 2D-Mo_2C, 2D-Mo_2C had much more exposed Mo sites (Fig. 11a), indicated by the high CO uptake up to 41.1 μmol g^{-1}. These exposed Mo sites acted as active sites to facilitate CO_2 adsorption and H_2 dissociation, boosting the activity of 2D-Mo_2C in RWGS.[51] Mo_2CT_x is an excellent catalyst for the WGS reaction,[100] but it is inactive in the RWGS reaction. However, 2D-Mo_2C, showing high activity in RWGS, has a poor catalytic performance in the WGS reaction. XANES data revealed that the Mo got oxidized under the WGS conditions, reaching an oxidation state close to Mo_2CT_x. The lower activity was then due to the mass transport limitations caused by the decreased interlayer distance.[51]

Meanwhile, the surface termination groups affect the oxidation states of the transition metal. Taking Mo_2CT_x and 2D-Mo_2C (without T_x) as an example, the original Mo_2CT_x has a Mo oxidation state of *ca.* +3.9. After the surface termination groups were released, the oxidation states of Mo decreased, leading to a Mo oxidation state of +0.5 in 2D-Mo_2C.[100] The oxidation states of the transition metal may determine the activity of the material in the catalysis. To be specific, if the oxygen coverage of 2D-Mo_2CO_x/SiO_2 was either too low or too high corresponding to the Mo oxidation states of *ca.* +0.2 and +5.5 (Fig. 11b), it was inactive in the DRM reaction. In contrast, 2D-Mo_2CO_x/SiO_2 with two-thirds oxygen coverage corresponding to a +4 Mo oxidation state was a kind of excellent catalyst in DRM, as evidenced by the DFT calculation.[98]

Surface termination groups also play an important role in forming acid-basic sites and active sites, which can promote the activity of reaction. Compared with β-Mo_2C, Brønsted or Lewis acid sites were observed on Mo_2CT_x, which could promote the dehydration of methanol to produce dimethyl ether (DME). Similar acidity was observed on 2D-Mo_2C, where T_x groups were completely removed.[51] Furthermore, the fluoro groups can strongly bond with transition metals in $Ti_3C_2T_x$ to form active Brønsted acid sites, while the surface oxygen groups were identified to be active basic sites (Fig. 11c). On the surface covered with these acid-basic pairs, furfural hydrogenation and guaiacol HDO were greatly promoted.[93,94]

3.5 Active sites

Active sites are typically the exposed transition metals or the unique structure of the metals and surface termination groups of MXenes. In contrast with termination groups, the regulation of active sites is a more direct way to improve the efficiency of thermal catalysis, because these sites will promote reactants to form free radical particles or reduce the reaction energy barriers.[127]

As for the function in facilitating the generation of free radical particles, the desulfurization reaction catalyzed by h-TC/TAC is a good example.[44,96] In this reaction, the –O and –OH termination groups produced in the alkaline selective etching can interact strongly with Ti to form Ti–O and Ti–OH structures, and in turn, these unique structures act as active centers to accelerate the oxygen molecular transformation into radicals. *In situ* electron spin resonance (ESR) spectroscopy revealed that the oxygen molecules were likely to be converted into $^{\bullet}OH$ and $^{\bullet}O_2^-$ radicals on these Ti–O and Ti–OH structures. Then these oxygen radicals would interact with DBT to further generate $DBTO_2$ (Fig. 12a).[44] In addition, Ti metal active sites in Ti_3C_2 MXenes also promoted the production of radicals in the thermal decomposition of ammonium perchlorate-based molecule perovskite ($(H_2dabco)[NH_4(ClO_4)_3]$, DAP-4).[128] In this case, the protons were transferred from H_2dabco^{2+} and NH^{4+} to ClO_4^- to generate dabco, NH_3, and $HClO_4$, respectively. Among these products, the oxygen atom in $HClO_4$ was further converted into the superoxide radical anion ($^{\bullet}O_2^-$) with the assistance of Ti sites (Fig. 12b). Under the action

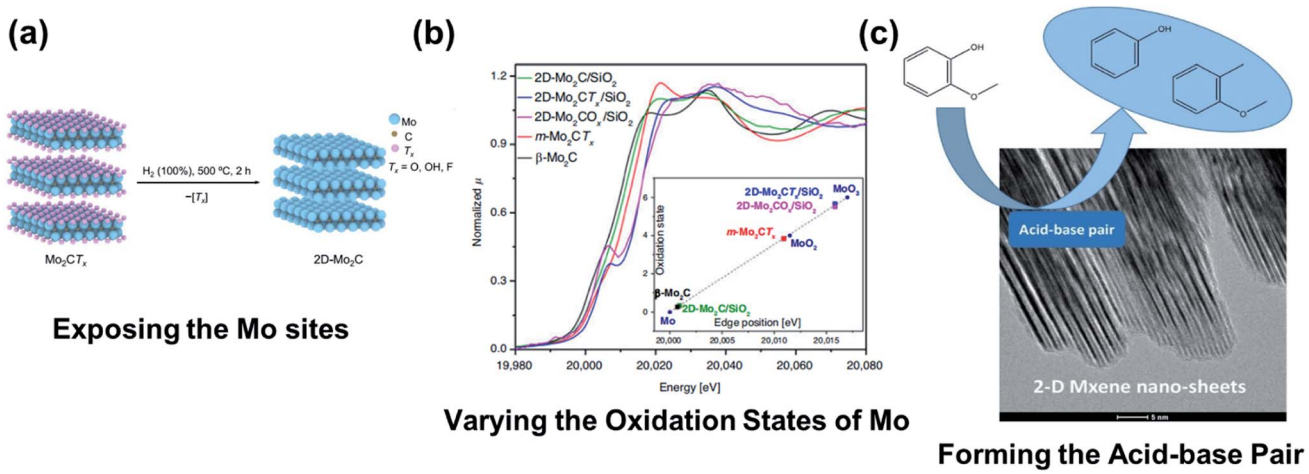

Fig. 11 Influence of surface terminations. (a) Schematic of the exposure of Mo sites in the formation of 2D-Mo_2C from Mo_2CT_x. Reproduced with permission.[51] Copyright 2021, Springer Nature. (b) Oxidation state of molybdenum in reference and synthesized materials determined from XANES spectra. Reproduced with permission.[98] Copyright 2020, Springer Nature. (c) The mechanism schematic diagram of producing phenol and methylanisole from guaiacol with the acid-basic pair. Reproduced with permission.[94] Copyright 2020, Elsevier.

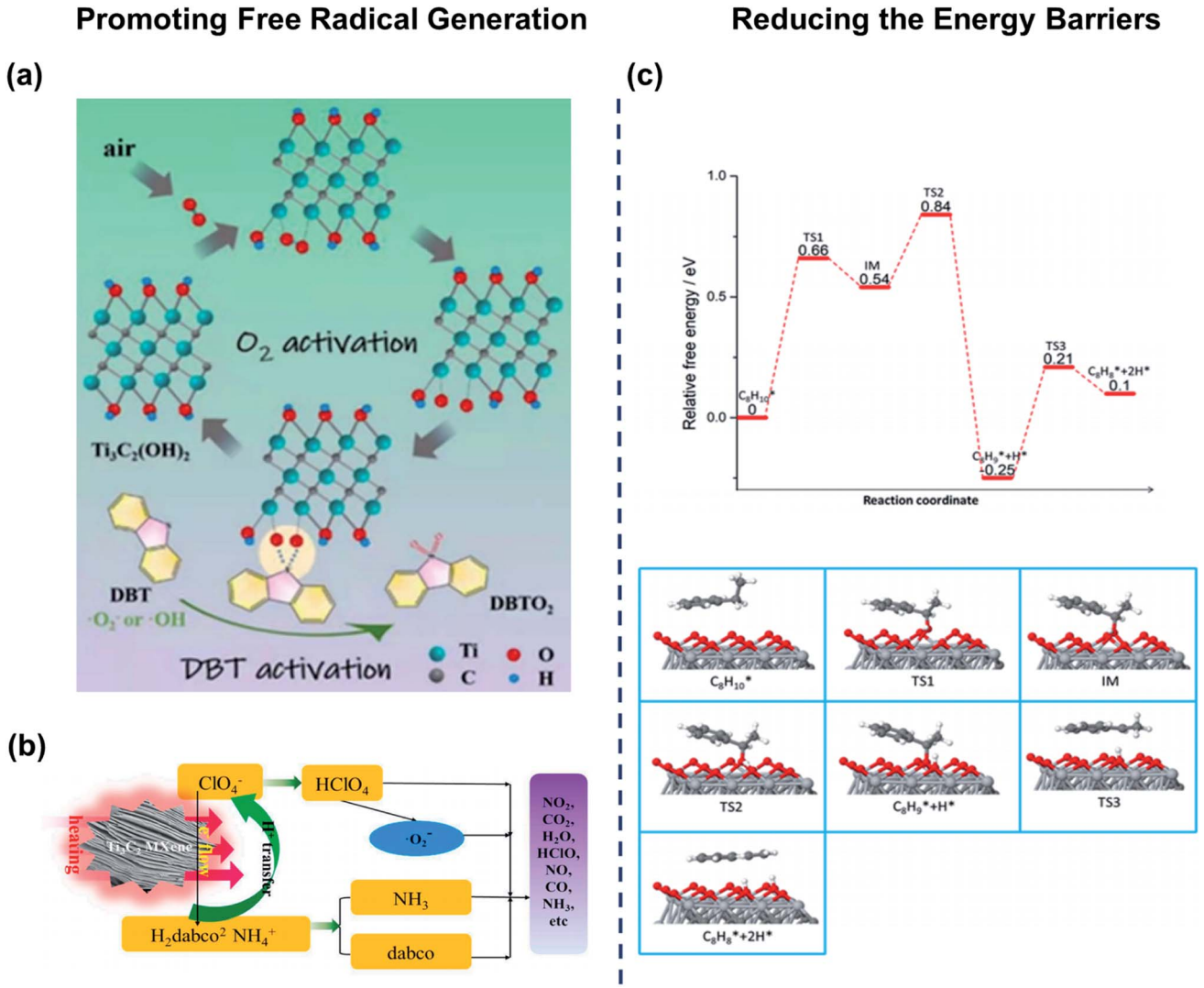

Fig. 12 The roles of active sites. (a) The DBT activation process under the action of $^{\bullet}O_2^-$ and $^{\bullet}OH$ radicals. Reproduced with permission.[44] Copyright 2020, Elsevier. (b) The thermal decomposition of DAP-4 with the assistance of $^{\bullet}O_2^-$. Reproduced with permission.[128] Copyright 2020, Elsevier. (c) The reaction pathway and important structures of ethylbenzene dehydrogenation on $Ti_3C_2O_2$. Ti is shown in light gray, C in dark gray, O in red, and H in white. Reproduced with permission.[95] Copyright 2018, American Chemical Society.

of $^{\bullet}O_2^-$, the cage structure of DAP-4 composed of NH^{4+}, ClO^{4-}, and H_2dabco^{2+} was destroyed completely which made the combustion reaction occur at a relatively low temperature (341.2 °C) compared with the reaction temperature of thermal decomposition of DAP-4 without any catalysts at 385 °C.

The active sites from MXene materials can decrease the energy barrier of the rate-limiting step. For example, José and co-workers used DFT to calculate the energy barrier of ammonia (NH_3) production catalyzed by 18 different MXenes including nine carbides and nine nitrides of which transition metals ranged from groups IV to group VI.[43] The result showed that with the assistance of hollow metal sites on the MXene (0001) surface, the dissociation of molecular nitrogen, the rate-limiting step for ammonia production, was greatly promoted due to its low energy barriers under 1 eV. W_2N was the most favorable type of MXene for this reaction with a dissociation energy barrier of only 0.28 eV, which was lower than that of Ru metal and a cesium-promoted ruthenium particle supported on MgO. Likewise, hydrogen abstraction, the rate-limiting step of the dehydrogenation reaction, was facilitated as well due to the reduced energy barriers. To be precise, on the oxygen-covered surface, the dissociation energies of the two hydrogen atoms in HCOOH were only 0.25 and 0.61 eV, respectively. Besides, the energies for breaking the two C–H bonds in EB were merely 0.66 and 0.46 eV, respectively (Fig. 12c).

Furthermore, the reduction of energy barriers can be realized by decreasing the adsorption energy, which was suggested by calculating the adsorption and dissociation energy barriers of water on a set of 18 M_2X MXenes (M = Ti, Zr, Hf, V, Nb, Ta, Cr, Mo, and W, while X = C or N).[129] It was shown that all the studied MXenes exothermically adsorbed water on their corresponding metal sites with the adsorption energies ranging from −1.43 to −2.94 eV, which was much lower compared with the ternary catalyst with Zn and Al atoms doped on Cu surfaces.

4. MXenes as supports

MXenes can not only serve as catalysts to directly provide active sites *via* their robust $M_{n+1}X_n$ frameworks and surface termination groups but also form more active heterogeneous catalysts by supporting transition metals (Table 2). The advantages of adopting MXenes as catalyst supports include their tunable surface properties[130] and outstanding stability,[131] which can offer the anchoring sites for transition metals and improve their anti-sintering ability.[132,133] Nanoparticles (NPs), nanoclusters, or single atoms can be formed on MXene supports according to the different sizes of the transition metals. In this section, we thoroughly summarize the reactions catalyzed by MXene-supported catalysts (Fig. 13) and explain the unique advantages of MXenes as supports. Furthermore, the metal–support interactions between transition metals and MXenes are explicated.

4.1 Transition metal nanoparticles (NPs)

Transition metal nanoparticles (TMNPs), the state between the bulk solid and molecular level, are the common loading form on MXenes,[139] due to their higher dispersion in solvent and 3D rotational freedom.[140,141] Combined with the strong catalytic activity from transition metals and the stability from MXenes,[136,137] MXene-supported catalysts can be obtained through some relatively simple preparation methods such as impregnation. In this part, we summarize the common way to load TMNPs on MXenes and further elaborate the application of these catalysts in thermal catalysis.

4.1.1 Synthesis. The most common way to generate MXene-supported TMNPs is impregnation. In this method, the catalyst supports are first immersed or soaked in a metal salt solution and then they are further activated to generate their corresponding active forms.[142] Heat treatment is a commonly used activation method. For example, Ma *et al.* used this method to prepare Co–$Ti_3C_2T_x$ MXene.[134] $Ti_3C_2T_x$ was soaked in cobalt nitrate hexahydrate, and the product obtained from the solution was thermally treated under N_2 and Ar atmospheres. The results showed that Co was deposited on MXenes in the form of rod-shaped Co_3O_4 with a crystal size of *ca.* 10.8 nm. Besides, nanocomposites can be activated *via* self-reduction reactions. For instance, Pt/$Ti_3C_2T_x$ can be prepared by dispersing it in a solution of H_2PtCl_6,[143] and the corresponding product was reduced with ammonia borane (NH_3BH_3). The results showed that the Pt TMNPs were clearly distributed on the $Ti_3C_2T_x$ surface with an average size of 2.2 nm. Furthermore, a $Ti_3C_2(-OH_xF_{1-x})_2$@AuNP composite was prepared by a similar process,[47] in which the MXenes were added into $HAuCl_4$ with the reducing agent of $NaBH_4$. Recently, this impregnation route was accelerated with the assistance of microwaves.[132] Under the

Table 2 The catalytic performance of MXene-supported catalysts

Catalyst	Reaction	Main reactant	T (°C)	P (MPa)	Conv.[a] (%)	Target product	Sel.[b] (%)	Ref.
Pd_{50}–Ru_{50}/$Ti_3C_2T_x$	CO_2 hydrogenation	CO_2	150	1.0	78	CH_3OH	76	132
Co–$Ti_3C_2T_x$	CO_2 hydrogenation	CO_2	400	0.1	15.7	CO	86.4	134
Co–$Ti_3C_2T_x$-NH_3	CO_2 hydrogenation	CO_2	400	0.1	45.1	CH_4	79.6	134
Pt_1/$Ti_{3-x}C_2T_x$	CO_2 functionalization	CO_2	140	0.1	100	Formamides	100	135
Cu/Mo_2CT_x/SiO_2	CO_2 hydrogenation	CO_2	230	2.5	3.2	CH_3OH	37	122
Pt/$Ti_3C_2T_x$	Light alkane dehydrogenation	Propane	550	0.1	15	Propylene	~95	136
Pt/Nb_2CT_x	Light alkane dehydrogenation	Propane	550	0.1	15	Propylene	~90	136
Pt/Nb_2CT_x	Water–gas shift reaction	CO	300	0.1	—	H_2	—	137
Pt/$Mo_2TiC_2T_x$	Non-oxidative coupling of methane	CH_4	750	0.1	7	C_2 products	>98	138

[a] Conversion refers to the conversion of the main reactant. [b] Selectivity refers to the selectivity of the target product.

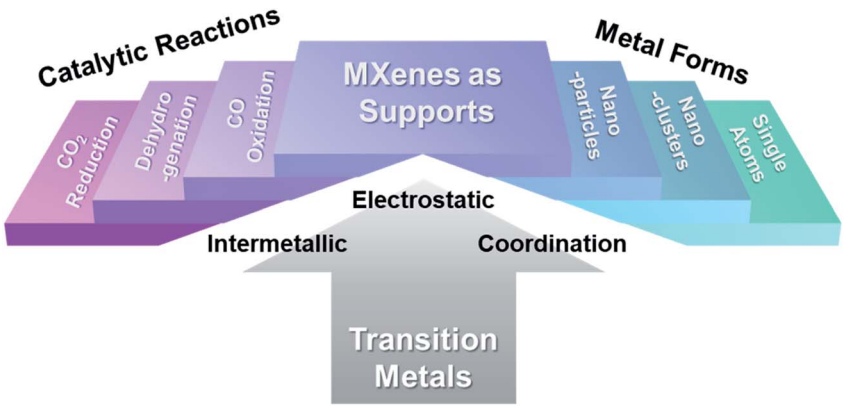

Fig. 13 Catalysts formed by the interactions between MXene supports and metals and their applications in thermal catalysis.

microwaves, $PdCl_2$, $RuCl_3 \cdot xH_2O$ salts, and $NaBH_4$ were added to the $Ti_3C_2T_x$ colloidal solution in turn. In this case, metallic Pd and Ru nucleation seeds were formed on $Ti_3C_2T_x$, which favored the formation of Pd_{50}–Ru_{50} alloy particles. Eventually, the individual Pd_{50}–Ru_{50} particles displayed a highly agglomeration-free homogeneous dispersion on $Ti_3C_2T_x$ with an average diameter of 3.2 nm.

4.1.2 Applications in thermal catalysis. MXenes especially $Ti_3C_2T_x$ usually act as supports to improve the activity and stability of the catalysts in CO_2 reduction and dehydrogenation of hydrogen carriers. Pd_{50}–$Ru_{50}/Ti_3C_2T_x$ has been used in the CO_2 hydrogenation process in which $NaBH_4$ served as a H_2 donor and ethylene glycol (EG) solution acted as a capture agent.[132] Under the optimal reaction conditions (at 120 °C for 12 h in a mixed solution of EG and water with a volume ratio of 18 : 2, and hydrogen was provided by 1 mol $NaBH_4$), the Pd_{50}–$Ru_{50}/Ti_3C_2T_x$ catalyst produced a higher CO_2 conversion efficiency of 78% with a CH_3OH yield of 76%. In contrast, $Ti_3C_2T_x$ and Pd_{50}–Ru_{50} displayed a CH_3OH yield of 23% and 52%, and a total CO_2 conversion of 28% and 57%, respectively (Fig. 14a). The superior catalytic effect stemmed from the synergy of the Pd_{50}–Ru_{50} alloy and $Ti_3C_2T_x$, in which the Ti–O basic pair on $Ti_3C_2T_x$ facilitated the adsorption of CO_2. Meanwhile, the interface between Pd_{50}–Ru_{50} and MXenes was suitable for adsorbing H_2 to generate H* atoms. After the adsorption process, the reactive H* atoms diffused to the vicinity of adsorbed CO_2 molecules to generate HCOO* followed by the formation of H_2COO*. The H_2COO* would then react with excessive H* atoms to form H_2CO* associated with water molecules, resulting in methanol formation (Fig. 14b). Moreover, it has also been reported that the Pd_{50}–$Ru_{50}/Ti_3C_2T_x$ catalyst showed remarkable chemical stability even after prolonged use for CO_2 hydrogenation.

Co–$Ti_3C_2T_x$ was another catalyst applied in catalyzing CO_2 reduction, and this catalyst realized tunable selectivity during CO_2 hydrogenation by modifying the MXene support.[134] In Co–$Ti_3C_2T_x$, CO was the main product with a reaction rate of 10.6 μmol g_{cat}^{-1} s^{-1} and a selectivity of up to 86.4%, which was about three times higher than the CO selectivity of Co/TiO_2 and Co/TiC. However, if N was doped on Co–$Ti_3C_2T_x$ through NH_3 treatment, denoted as Co–$Ti_3C_2T_x$–NH_3, CH_4 would be the more accessible product with a formation rate of 30.4 μmol g_{cat}^{-1} s^{-1}. Co–$Ti_3C_2T_x$–NH_3 exhibited a CH_4 selectivity of 79.6% and a CO selectivity of 20.4% (Fig. 14c). This change stemmed from the enhanced reducibility of the catalyst surface. Specifically, after N was doped on MXenes by partially substituting C, MXenes would become unstable and TiO_2 emerged on MXenes. The produced TiO_2 strongly interacted with Co nanoparticles

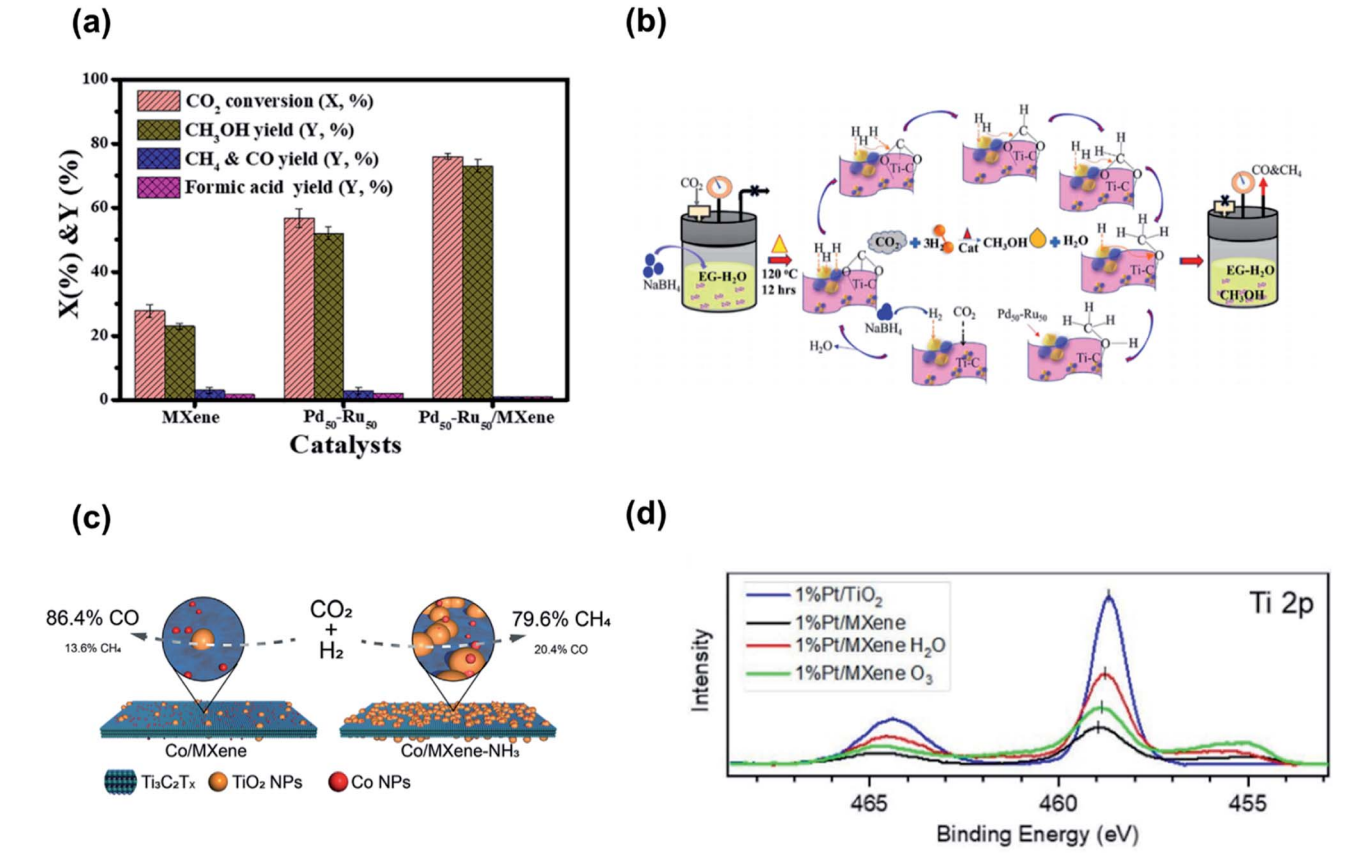

Fig. 14 The applications of MXene-supported nanoparticle catalysts. (a) The CO_2 hydrogenation with MXene, Pd_{50}–Ru_{50}, and Pd_{50}–Ru_{50}/MXene. (b) Schematic illustration of the hydrogenation of CO_2 to methanol on the Pd_{50}–$Ru_{50}/Ti_3C_2T_x$ catalyst. Reproduced with permission.[132] Copyright 2021, Elsevier. (c) The reaction pathway over cobalt NPs supported on MXenes. Reproduced with permission.[134] Copyright 2021, Wiley-VCH. (d) Ti 2p XPS spectra of 1 wt% Pt-loaded catalysts. Reproduced with permission.[144] Copyright 2020, IOP.

and the strong interaction made the reducibility of Co nanoparticles at the interface of the TiO_2 nanoparticles increase, resulting in the shift of product selectivity from CO to CH_4.

Modified MXenes can serve as important supports for dehydrogenation reactions occurring on hydrogen carriers. For instance, Pd/PDA–$Ti_3C_2T_x$ was a superior catalyst to catalyze the formic acid dehydrogenation process, wherein the carrier, PDA–$Ti_3C_2T_x$, was prepared by alkalization of *p*-phenylenediamine (PDA), and Pd NPs were loaded on $Ti_3C_2T_x$ by impregnation.[145] This catalyst exhibited a good catalytic activity with a turnover frequency (TOF) value of up to 924.4 h^{-1}, which was 16 times higher than that of Pd/zeolite under similar conditions. The authors proposed that the excellent activity was mainly attributed to the improved synergistic effect between PDA-MXenes and Pd NPs. The PDA together with surface termination groups on MXenes had a scavenging effect on protons, which promoted the dissociation process of the O–H bond in formic acid to generate formate intermediates. Meanwhile the Pd TMNPs provided adsorption sites for formate intermediates and generated palladium formate complexes. On these Pd sites, the C–H bonds of formate intermediates were broken, producing Pd–H and CO_2, and the H of Pd–H species can be further released to produce H_2.

Another commonly used modification method was oxidation. For instance, $Ti_3C_2T_x$ oxidized by O_3 can act as carriers to support Pt NPs to boost the effectiveness of the hydrolysis of ammonia borane.[144] Pt supported on untreated $Ti_3C_2T_x$ (Pt/$Ti_3C_2T_x$) or commercial TiO_2 (Pt/TiO_2) gave a TOF of 39 and 38 min^{-1}, respectively, whereas supporting Pt on ozone-treated $Ti_3C_2T_x$ (Pt/$Ti_3C_2T_x$–O_3) increased the TOF by seven times to 265 min^{-1}. Although Pt/$Ti_3C_2T_x$–H_2O obtained *via* hydrothermal treatment featured a high TOF similar to Pt/$Ti_3C_2T_x$–O_3, the activation energy of this material was up to 99 kJ mol^{-1}. This superior catalytic performance was due to electronic interactions between the particles and the modified oxide surface. On the MXene surface, electrons tended to transfer from the TiO_2 layer to the supported particle, making the Pt more electron-deficient with a higher oxidation state (Fig. 14d). Therefore, electron-rich ammonia borane was more likely to be adsorbed on the electron-deficient Pt surface, resulting in lower binding energy.

4.2 Transition metal nanoclusters (NCs) or single atoms (SAs)

Unlike catalysts loaded with NPs, NCs and SACs are usually dispersed atomically on carriers with coordinative unsaturation,[146] making these catalysts have the maximum atomic utilization.[138,147–149] Unfortunately, the large-scale synthesis of catalysts loaded with NCs or SACs remains a challenge due to the natural tendency for metal atoms to diffuse and agglomerate.[150] In contrast, MXenes can provide numerous dispersed sites for uniform deposition of NCs and SACs through their termination groups and vacancy defects. Therefore, the agglomeration of metal atoms can be avoided, making the MXenes loaded with NCs or SAs become a novel kind of efficient catalyst.[137] In this section, we exemplify the synthesis methods of this kind of catalyst and provide evidence from both experimental and computational levels that MXene-supported single-atom and atom-cluster catalysts feature strong catalytic activity in various reactions.

4.2.1 Synthesis. Through the surface organometallic chemistry (SOMC) approach followed by H_2 treatment, Cu SAs and NCs were loaded on Mo_2CT_x.[122] $Mo_2CT_x/SiO_{2\text{-}500}$, the catalyst carrier, was generated by impregnating 2D-Mo_2CT_x on SiO_2, followed by the dehydroxylated process at 500 °C under a N_2 flow. CuMes [Cu_n(mesityl)$_n$, n = 2, 4, 5] were grafted onto ≡SiOH sites by dispersing $Mo_2CT_x/SiO_{2\text{-}500}$ in a mixture solution of toluene and [Cu_5(mesityl)$_5$]. Then the grafted CuMes precursor was decomposed and migrated from the ≡SiOH sites to 2D-Mo_2CT_x by exposing this grafted material in H_2 at 500 °C for 2 h, and the obtained products were denoted as Cu/Mo_2CT_x/$SiO_{2\text{-}2h}$. Interestingly, the diameter of Cu on the SiO_2 surface was approximately 3 nm. In contrast, the Cu on the Mo_2CT_x nanosheets had a higher dispersion, forming few-atom-small clusters and single Cu atoms. Although this method can obtain MXene-supported catalysts loaded with Cu NCs and SAs efficiently, the synthetic process was relatively complicated. $Pt_1/Ti_{3-x}C_2T_x$ catalysts can be prepared by a relatively simple simultaneous self-reduction stabilization process with the help of Ti vacancies under milder conditions.[135] The $H_2PtCl_6 \cdot 6H_2O$ solution with $[PtCl_6]^{2-}$ complex ions was injected into the MXene suspension under stirring, and the $[PtCl_6]^{2-}$ ions were uniformly adsorbed onto the surface of $Ti_{3-x}C_2T_x$ flakes. In this case, Pt^{4+} in $[PtCl_6]^{2-}$ was slowly reduced by the highly unstable and reductive Ti vacancies, and $Pt_1/Ti_{3-x}C_2T_x$ was successfully produced. The formed Pt SAs were uniformly located on Ti vacancies of the $Ti_{3-x}C_2T_x$ nanosheet by substitution instead of just interstitial doping.

4.2.2 Applications in thermal catalysis. Researchers have demonstrated that MXene-supported single-atom or atom-cluster catalysts have high activity for CO_2 reduction. For example, Zhao *et al.* built a Pt-loaded single-atom catalyst ($Pt_1/Ti_{3-x}C_2T_x$) which offered a green route to utilize greenhouse gas *via* the formylation of amines, silane, and CO_2.[135] $Pt_1/Ti_{3-x}C_2T_x$ shows nearly 100% formamides yield, much higher than the yield with Pt NPs. DFT calculations proved that $Pt_1/Ti_{3-x}C_2T_x$ showed a relatively lower barrier energy in CO_2 insertion into a Pt–H bond (TS1), the aniline reaction (TS2), and the reductive elimination (TS3) process (Fig. 15a). The authors speculated that the partially positively charged Pt single atoms appeared to decrease the larger steric hindrance in the adsorption of aniline, and simultaneously reduce the energy barrier to active silane, CO_2, and aniline, thereby boosting catalytic performance.

Converting CO_2 into methanol is another way to utilize CO_2 efficiently. Zhou *et al.* engineered Cu/Mo_2CT_x/SiO_2 to selectivity boost CO_2 methanolization (Fig. 15b).[122] The activity of Cu/$Mo_2CT_x/SiO_{2\text{-}2h}$ was much higher than that of the industrial Cu-based methanol synthesis catalyst Cu–ZnO–Al_2O_3. Besides, the intrinsic methanol formation rate of Cu/$Mo_2CT_x/SiO_{2\text{-}2h}$ was 1.51 g h^{-1} g_{Cu}^{-1}, around three times higher than that of Cu/$SiO_{2\text{-}2h}$. Through prolonging the reduction time to 6 h in H_2, the Cu/$Mo_2CT_x/SiO_{2\text{-}6h}$ catalyst possessed a higher Cu dispersion compared with Cu/$Mo_2CT_x/SiO_{2\text{-}2h}$, resulting in a higher

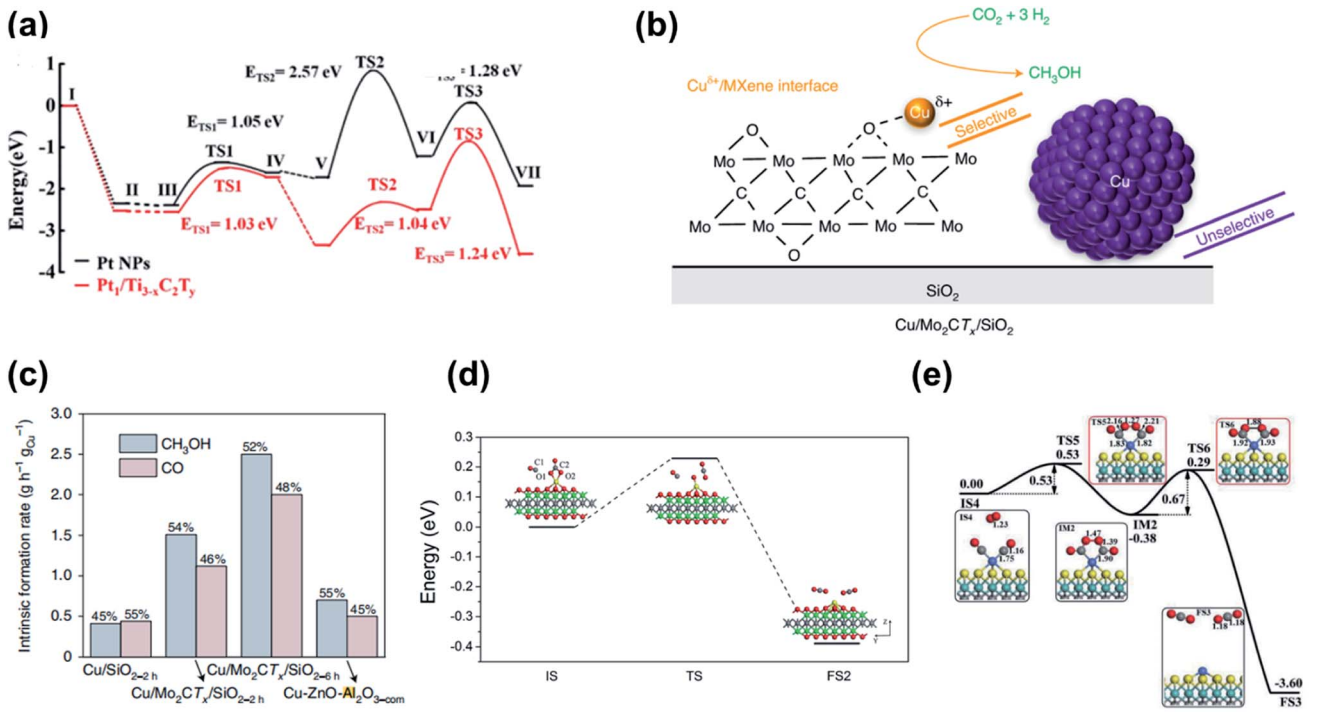

Fig. 15 The applications of MXene-supported nanocluster and single-atom catalysts. (a) Calculated energy profiles for $Pt_1/Ti_{3-x}C_2T_x$ (red line) and Pt NPs (black line). Reproduced with permission.[135] Copyright 2019, American Chemical Society. (b) Schematic of $Cu/Mo_2CT_x/SiO_2$ to selectively promote CO_2 methanolization. (c) Comparison of the intrinsic formation rates of CH_3OH and CO with the different catalysts. Reproduced with permission.[122] Copyright 2021, Springer Nature. (d) CO oxidation on the Ti-anchored Ti_2CO_2 monolayer *via* the ER mechanism. Reproduced with permission.[151] Copyright 2016, Royal Society of Chemistry. (e) Energy profile and optimized structure of the corresponding stationary points for CO oxidation with Co_1/Mo_2CS_2 by the TER mechanism. The units of energies and bond lengths are eV and Å separately. Reproduced with permission.[49] Copyright 2021, Springer.

intrinsic methanol formation rate of 2.49 g h^{-1} g_{Cu}^{-1} (Fig. 15c). The increased catalytic performance originated from the unique interface formed by the interaction between Cu and Mo_2CT_x. In this interface, the Cu atom and the support both participated in the reaction by reducing the energy barriers for successive heterolytic cleavages of H_2 required to form HCOO*, H_2COO*, and H_2COOH* species. Therefore, the formation of the H_2COO* species, the most energy-demanding step in the methanol production pathway, occurred easily. Hence, on $Cu/Mo_2CT_x/SiO_{2\text{-}6h}$, CH_3OH was more easily obtained under CO_2 hydrogenation conditions.

Researchers also proved that MXene-supported single-atom and atom-cluster catalysts can greatly decrease the energy barriers in CO oxidation. Zhang *et al.* discovered a Ti-anchored Ti_2CO_2 monolayer as a single-atom catalyst for CO oxidation.[151] The calculation result proved that the reaction was more likely to occur under the Eley–Rideal (ER) mechanism with an energy barrier of 0.23 eV, which was lower than the energy barrier of many noble metal catalysts such as Pt/FeO_x. In this reaction, the physically adsorbed CO was inserted into the O–O bond of the pre-adsorbed O_2 to form a carbonate-like intermediate. Subsequently, another CO molecule was absorbed in the vicinity of a carbonate-like intermediate and transformed into CO_2 (Fig. 15d). The evaluation of Ti-anchored MXene catalysts showed that Ti was adsorbed stably on the Ti_2CO_2 substrate with an energy of −7.68 eV. Co_1/Mo_2CS_2 was another efficient catalyst to accelerate the oxidation of CO, because it can lower the energy barriers of the rate-limiting step in the Termolecular Eley–Rideal (TER) mechanism, *i.e.*, the formation of two CO molecules from the dissociation of the OCO–Co–OCO intermediate, with an energy barrier of only 0.67 eV (Fig. 15e).[49] Moreover, oxygen vacancies played a significant role in CO oxidation. For instance, the oxygen vacancy in Pd-deposited Mo_2CO_2 can stabilize the single Pd atom, making the Pd/O_V–Mo_2CO_2 system remain an excellent mono-dispersed atomic catalyst in the reaction.[152]

4.3 Metal–support interactions between transition metals and MXenes

By combining the unique properties of metals (in the form of NPs, SAs, and NCs) and MXenes, metal-based catalysts supported by MXenes may be promising in thermal catalysis. While the strong and stable connection between metals and MXenes is usually ignored, it is the prerequisite for the stable use of this kind of catalyst, and therefore, more and more studies start to focus on metal–support interactions. Currently, there are three kinds of interactions for MXene-supported catalysts: (i) electrostatic interaction,[132] (ii) intermetallic interaction,[138] and (iii) coordination interaction.[122] Due to these three kinds of interactions, the synergistic effects in catalysis between a transition metal and MXenes can be obtained, and the stability of MXene-

supported catalysts is greatly enhanced.[153] Therefore, in this section, we first summarize the main interactions between transition metals and MXenes. The effect of the interactions on catalyst properties and catalytic performance is further explained.

Among the numerous MXene-supported catalysts loaded with TMNPs, metal–support interactions usually exist in the form of electrostatic attraction force, which typically originates from the impregnation process. Specifically, when MXenes like Pd_{50}–$Ru_{50}/Ti_3C_2T_x$ (Fig. 16a) were immersed in metal salt solutions, positively charged metal ions were attracted by the negatively charged termination groups on MXenes.[132] After that, the metal ions can be reduced to metallic particles *in situ* with a reducing agent or heat treatment.[132] Furthermore, some stronger electrostatic interactions can be obtained on modified MXenes with NPs loaded, such as $Pt/Ti_3C_2T_x$–O_3.[144] On these surfaces of MXenes, Ti in unsaturated oxide states including Ti^{2+} and Ti^{3+} was transformed into TiO_2. When the TMNPs approached the TiO_2, strong connections between the MXenes and the NPs occurred, due to the electron tending to transfer from TiO_2 to Pt. Besides, the intermetallic phase was another stable interaction, which emerged on $Pt/Ti_3C_2T_x$ and Pt/Nb_2CT_x treated with H_2.[136] Under a hydrogen atmosphere, fully exposed Ti or Nb strongly interacted with Pt to form a highly regular intermetallic compound (IMC), Pt_3Ti, *via* reactive metal–support interactions (RMSI) (Fig. 16b). This compound was composed of periodic hexagonal arrays of Pt atoms surrounded by Ti atoms at the center of the hexagons (Fig. 16c). For SA- and NC-based catalysts, coordination bonds are the predominant force in the metal–MXene interaction. Carbon atoms in MXenes act as ligands to provide bonding electrons, while supported metals provide empty orbitals to form stable covalent bond structures. For instance, on $Cu/Mo_2CT_x/SiO_2$, Cu atoms located on the edges of Mo_2CT_x were speculated to be connected with MXenes through coordination.[122] It was likely that surface μ-oxo sites (Mo–O–Mo) of Mo_2CT_x interacted with Cu^0 by forming Mo–O–Cu^+ linkages (Fig. 16d). Similarly, in $Pt_1/Ti_{3-x}C_2T_x$, the single Pt atoms were stabilized in the Ti vacancies and then coordinated with three carbon atoms on the MXene nanosheets.[135]

Strong metal–MXene interaction can promote the stability of the catalysts, and meanwhile, the electronic properties of MXene-supported catalysts are modified, for the reason that the interfaces of the stable metal–MXenes catalysts provide a bridge for electron transfer and rearrangement in both transition metals and MXene carriers, thus forming more active catalysts. For instance, the interaction between the Cu_3 cluster and monolayer defective Mo_2CO_2 (d-Mo_2CO_2) made Cu_3 clusters act as an electron reservoir to boost the catalysis of CO oxidation.[48] Before O_2 adsorption, the doped Cu_3 cluster functioned as an electron reservoir to collect electrons from defective Mo_2CO_2,

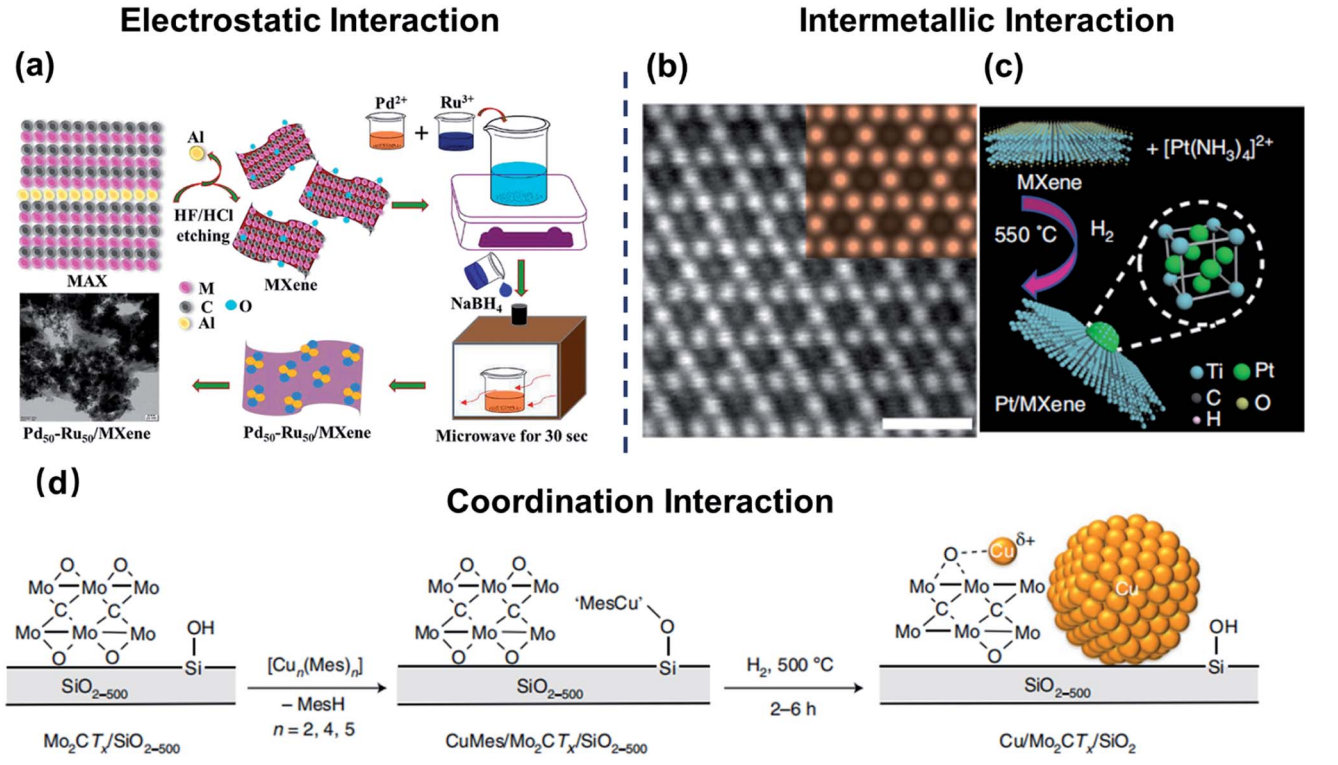

Fig. 16 The metal–support interactions between transition metals and MXenes. (a) Schematic illustration of the preparation of MXenes from MAX *via* HF/HCl etching and loading Pd_{50}–Ru_{50} TMNPs by electrostatic interaction. Reproduced with permission.[132] Copyright 2021, Elsevier. (b) The (111) surface of Pt_3Ti NP. (Inset) A simulated STEM image of the Pt_3Ti (111) surface. (c) Schematic of RMSI in Pt/MXene catalysts and the structure of $L1_2$-ordered intermetallic Pt_3Ti. Reproduced with permission.[136] Copyright 2018, Springer Nature. (d) The synthesis of $Cu/Mo_2CT_x/SiO_{2\text{-}500}$ with highly dispersed Cu sites in coordination interaction with partially reduced Mo_2CT_x nanosheets. Reproduced with permission.[122] Copyright 2021, Springer Nature.

while it donated electrons when adsorbing O_2 and CO. To be precise, some electrons were transferred from Cu atoms to occupy the empty 2π*-antibonding orbits of gas-phase O_2 and CO, resulting in lower adsorption energy of O_2 and CO. In addition, the variation of electronic properties also occurred on $Pt/Ti_3C_2T_x$ when it acted as an efficient catalyst for light alkane dehydrogenation (LADH).[143] During the synthesis of $Pt/Ti_3C_2T_x$, Pt_3Ti intermetallic phase would be formed with a lower d band center. This change resulted in the weaker adsorption of light hydrocarbon species and changed the relative free energy and barriers of the reaction steps of LADH.

5. Summary and outlook

In summary, MXenes with a robust $M_{n+1}X_n$ skeleton and tunable surface termination groups have gradually attracted interest from the researchers in thermal catalysis, due to their noble-metal-like catalytic activity and high thermal stability. Among them, $Ti_3C_2T_x$, Mo_2CT_x, and V_2CT_x are the three most widely studied MXenes in thermal catalysis, which can usually be obtained through a HF selective etching process. They can act as catalysts to directly participate in thermal reactions like hydrogenation, dehydrogenation, CO oxidation, *etc.* Their catalytic performance, such as stability and selectivity, can be adjusted by varying the types and the coverage of the surface termination groups, owing to the role of T_x groups in adjacent atoms and surface properties. Meanwhile, the efficiency of the reaction can also be directly boosted through the unique design of the active sites on the surface of MXenes, which would mainly facilitate the decrease of the energy barriers of the reactants. Besides, MXenes can also serve as catalytic carriers to support TMs in the form of NPs, NCs, and SAs, which can further improve the stability of the catalysts compared with traditional metal-based catalysts. In particularly, through metal–support interaction including electrostatic interaction, intermetallic interaction, and coordination interaction, a bridge between TMs and MXenes can be built to transfer the electrons, resulting in the rearrangement of the electrons in catalysts and thus improving the catalytic activity.[154]

Although MXenes in thermal catalysis have been investigated extensively, these materials are still facing some obstacles in practical applications. One of the major problems is the long-term stability, because MXenes are quite sensitive to both water and oxygen. Meanwhile, considering that harsh conditions like high temperature and high pressure are usually required in thermal catalysis, the acceleration of the deactivation of MXenes will commonly occur. Therefore, the synthesis of extremely stable MXene-based catalysts, which can catalyze reactions under milder conditions, should be explored. Moreover, the cost and the security in the synthesis of MXenes are worthy of attention, and low cost and environmentally friendly fluorine-free preparation routes instead of the HF etching method for MXene synthesis are desired. More importantly, there is still a lack of standards and protocols that could point out how to design more efficient MXene catalysts. Currently, DFT is widely applied to design and assess the structure of catalysts before the actual catalysis is performed.[38] However, the DFT investigation of MXenes in thermal catalysis is rather limited. More modelling and calculations ought to be performed to systematically forecast the catalytic performance of MXenes, which can better guide the preparation of MXenes-based catalysts.

Conflicts of interest

There are no conflicts to declare.

Acknowledgements

This work was supported by the Huaneng Group Science and Technology Research Project (KTHT-U22YYJC12), Tsinghua University-Shanxi Clean Energy Research Institute Innovation Project Seed Fund, and Tsinghua University Initiative Scientific Research Program (20213080042).

References

1 X. Jiang, A. V. Kuklin, A. Baev, Y. Ge, H. Ågren, H. Zhang and P. N. Prasad, *Phys. Rep.*, 2020, **848**, 1–58.
2 Y. Gogotsi and B. Anasori, *ACS Nano*, 2019, **13**, 8491–8494.
3 Y. Wang, J. Mao, X. Meng, L. Yu, D. Deng and X. Bao, *Chem. Rev.*, 2019, **119**, 1806–1854.
4 Y. Chen, Z. Fan, Z. Zhang, W. Niu, C. Li, N. Yang, B. Chen and H. Zhang, *Chem. Rev.*, 2018, **118**, 6409–6455.
5 M. Liu, P. Zhang, Z. Qu, Y. Yan, C. Lai, T. Liu and S. Zhang, *Nat. Commun.*, 2019, **10**, 3917.
6 Y. Yan, P. Zhang, Z. Qu, M. Tong, S. Zhao, Z. Li, M. Liu and Z. Lin, *Nano Lett.*, 2020, **20**, 7662–7669.
7 Y. Yan, S. Liang, X. Wang, M. Zhang, S. Hao, X. Cui, Z. Li and Z. Lin, *Proc. Natl. Acad. Sci. U. S. A.*, 2021, **118**, e2110036118.
8 X. Cai, Y. Luo, B. Liu and H. M. Cheng, *Chem. Soc. Rev.*, 2018, **47**, 6224–6266.
9 Y. Xue, G. Zhao, R. Yang, F. Chu, J. Chen, L. Wang and X. Huang, *Nanoscale*, 2021, **13**, 3911–3936.
10 S. Shirvani, M. Ghashghaee and K. J. Smith, *Catal. Rev.*, 2021, 1–51, DOI: 10.1080/01614940.2021.1899605.
11 K. Hantanasirisakul and Y. Gogotsi, *Adv. Mater.*, 2018, **30**, 1804779.
12 M. Naguib, O. Mashtalir, J. Carle, V. Presser, J. Lu, L. Hultman, Y. Gogotsi and M. W. Barsoum, *ACS Nano*, 2012, **6**, 1322–1331.
13 B. Anasori, M. R. Lukatskaya and Y. Gogotsi, *Nat. Rev. Mater.*, 2017, **2**, 16098.
14 J. Lei, X. Zhang and Z. Zhou, *Front. Phys.*, 2015, **10**, 276–286.
15 N. K. Chaudhari, H. Jin, B. Kim, D. San Baek, S. H. Joo and K. Lee, *J. Mater. Chem. A*, 2017, **5**, 24564–24579.
16 I. M. Chirica, A. G. Mirea, T. Nea U, M. Florea, M. W. Barsoum and F. Nea U, *J. Mater. Chem. A*, 2021, **9**, 19589–19612.
17 M. Shekhirev, C. E. Shuck, A. Sarycheva and Y. Gogotsi, *Prog. Mater. Sci.*, 2021, **120**, 100757.

18 J. Zhu, E. Ha, G. Zhao, Y. Zhou, D. Huang, G. Yue, L. Hu, N. Sun, Y. Wang, L. Y. S. Lee, C. Xu, K. Wong, D. Astruc and P. Zhao, *Coord. Chem. Rev.*, 2017, **352**, 306–327.
19 P. O. Å. Persson and J. Rosen, *Curr. Opin. Solid State Mater. Sci.*, 2019, **23**, 100774.
20 A. Agresti, A. Pazniak, S. Pescetelli, A. Di Vito, D. Rossi, A. Pecchia, M. Auf Der Maur, A. Liedl, R. Larciprete, D. V. Kuznetsov, D. Saranin and A. Di Carlo, *Nat. Mater.*, 2019, **18**, 1228–1234.
21 B. Ahmed, A. E. Ghazaly and J. Rosen, *Adv. Funct. Mater.*, 2020, **30**, 2000894.
22 F. Song, G. Li, Y. Zhu, Z. Wu, X. Xie and N. Zhang, *J. Mater. Chem. A*, 2020, **8**, 18538–18559.
23 C. Feng, Z. P. Wu, K. W. Huang, J. Ye and H. Zhang, *Adv. Mater.*, 2022, 2200180.
24 M. M. Hasan, M. M. Hossain and H. K. Chowdhury, *J. Mater. Chem. A*, 2021, **9**, 3231–3269.
25 X. Zhan, C. Si, J. Zhou and Z. Sun, *Nanoscale Horiz.*, 2020, **5**, 235–258.
26 D. Xiong, Y. Shi and H. Y. Yang, *Mater. Today*, 2021, **46**, 183–211.
27 D. Johnson, Z. Qiao, E. Uwadiunor and A. Djire, *Small*, 2022, **18**, 2106129.
28 Q. Tang, Z. Zhou and P. Shen, *J. Am. Chem. Soc.*, 2012, **134**, 16909–16916.
29 X. Li, C. Wang, Y. Cao and G. Wang, *Chem.–Asian J.*, 2018, **13**, 2742–2757.
30 F. Shahzad, M. Alhabeb, C. B. Hatter, B. Anasori, H. S. Man, C. M. Koo and Y. Gogotsi, *Science*, 2016, **353**, 1137–1140.
31 S. Kim, F. Gholamirad, M. Yu, C. M. Park, A. Jang, M. Jang, N. Taheri-Qazvini and Y. Yoon, *Chem. Eng. J.*, 2021, **406**, 126789.
32 X. Meng, X. Cui, N. P. Rajan, L. Yu, D. Deng and X. Bao, *Chem*, 2019, **5**, 2296–2325.
33 N. H. Ahmad Junaidi, W. Y. Wong, K. S. Loh, S. Rahman and W. R. W. Daud, *Int. J. Energy Res.*, 2021, **45**, 15760–15782.
34 H. Wang, Y. Wu, X. Yuan, G. Zeng, J. Zhou, X. Wang and J. W. Chew, *Adv. Mater.*, 2018, **30**, 1704561.
35 Q. Zhong, Y. Li and G. Zhang, *Chem. Eng. J.*, 2021, **409**, 128099.
36 H. Huang, X. Jiang, N. Li, D. Chen, Q. Xu, H. Li, J. He and J. Lu, *Appl. Catal., B*, 2021, **284**, 119754.
37 Q. Zhu, Y. Cui, Y. Zhang, Z. Cao, Y. Shi, J. Gu, Z. Du, B. Li and S. Yang, *Mater. Today Nano*, 2021, **13**, 100104.
38 Á. Morales-García, F. Calle-Vallejo and F. Illas, *ACS Catal.*, 2020, **10**, 13487–13503.
39 R. B. Levy and M. Boudart, *Science*, 1973, **181**, 547–549.
40 J. H. Sinfelt and D. J. C. Yates, *Nat. Phys. Sci.*, 1971, **229**, 27–28.
41 T. Hou, Q. Luo, Q. Li, H. Zu, P. Cui, S. Chen, Y. Lin, J. Chen, X. Zheng, W. Zhu, S. Liang, J. Yang and L. Wang, *Nat. Commun.*, 2020, **11**, 4251.
42 Z. Li and Y. Wu, *Small*, 2019, **15**, 1804736.
43 J. D. Gouveia, Á. Morales-García, F. Viñes, J. R. B. Gomes and F. Illas, *ACS Catal.*, 2020, **10**, 5049–5056.
44 Q. Zhang, J. He, X. Fu, S. Xie, R. Fan, H. Lai, W. Cheng, P. Ji, J. Sheng, Q. Liao, W. Zhu and H. Li, *Chem. Eng. J.*, 2022, **430**, 132950.
45 D. A. Kuznetsov, Z. Chen, P. V. Kumar, A. Tsoukalou, A. Kierzkowska, P. M. Abdala, O. V. Safonova, A. Fedorov and C. R. Müller, *J. Am. Chem. Soc.*, 2019, **141**, 17809–17816.
46 X. Yang, Z. Lu, C. Cheng, Y. Wang, X. Zhang, Z. Yang and W. Lu, *J. Phys. Chem. C*, 2020, **124**, 4090–4100.
47 K. Li, T. Jiao, R. Xing, G. Zou, J. Zhou, L. Zhang and Q. Peng, *Sci. China Mater.*, 2018, **61**, 728–736.
48 C. Cheng, X. Zhang, Z. Yang and Z. Zhou, *ACS Appl. Mater. Interfaces*, 2018, **10**, 32903–32912.
49 S. H. Talib, S. Baskaran, X. Yu, Q. Yu, B. Bashir, S. Muhammad, S. Hussain, X. Chen and J. Li, *Sci. China Mater.*, 2021, **64**, 651–663.
50 S. Samanta and R. Srivastava, *Mater. Adv.*, 2020, **1**, 1506–1545.
51 H. Zhou, Z. Chen, E. Kountoupi, A. Tsoukalou, P. M. Abdala, P. Florian, A. Fedorov and C. R. Müller, *Nat. Commun.*, 2021, **12**, 5510.
52 L. H. Zhang, Y. Shi, Y. Wang and N. R. Shiju, *Adv. Sci.*, 2020, **7**, 1902126.
53 J. Nan, X. Guo, J. Xiao, X. Li, W. Chen, W. Wu, H. Liu, Y. Wang, M. Wu and G. Wang, *Small*, 2021, **17**, 1902085.
54 J. Halim, J. Palisaitis, J. Lu, J. Thörnberg, E. J. Moon, M. Precner, P. Eklund, P. O. Å. Persson, M. W. Barsoum and J. Rosen, *ACS Appl. Nano Mater.*, 2018, **1**, 2455–2460.
55 L. Wang, M. Han, C. E. Shuck, X. Wang and Y. Gogotsi, *Nano Energy*, 2021, **88**, 106308.
56 W. Hong, B. C. Wyatt, S. K. Nemani and B. Anasori, *MRS Bull.*, 2020, **45**, 850–861.
57 B. Ahmed, A. E. Ghazaly and J. Rosen, *Adv. Funct. Mater.*, 2020, **30**, 2000894.
58 J. L. Hart, K. Hantanasirisakul, A. C. Lang, B. Anasori, D. Pinto, Y. Pivak, J. T. van Omme, S. J. May, Y. Gogotsi and M. L. Taheri, *Nat. Commun.*, 2019, **10**, 522.
59 L. Gao, W. Bao, A. V. Kuklin, S. Mei, H. Zhang and H. Ågren, *Adv. Mater.*, 2021, **33**, 2004129.
60 M. Naguib, M. W. Barsoum and Y. Gogotsi, *Adv. Mater.*, 2021, **33**, 2103393.
61 M. Naguib, M. Kurtoglu, V. Presser, J. Lu, J. Niu, M. Heon, L. Hultman, Y. Gogotsi and M. W. Barsoum, *Adv. Mater.*, 2011, **23**, 4248–4253.
62 P. Lakhe, E. M. Prehn, T. Habib, J. L. Lutkenhaus, M. Radovic, M. S. Mannan and M. J. Green, *Ind. Eng. Chem. Res.*, 2019, **58**, 1570–1579.
63 M. Ghidiu, M. R. Lukatskaya, M. Zhao, Y. Gogotsi and M. W. Barsoum, *Nature*, 2014, **516**, 78–81.
64 C. Peng, P. Wei, X. Chen, Y. Zhang, F. Zhu, Y. Cao, H. Wang, H. Yu and F. Peng, *Ceram. Int.*, 2018, **44**, 18886–18893.
65 L. Wang, H. Zhang, B. Wang, C. Shen, C. Zhang, Q. Hu, A. Zhou and B. Liu, *Electron. Mater. Lett.*, 2016, **12**, 702–710.
66 J. Halim, M. R. Lukatskaya, K. M. Cook, J. Lu, C. R. Smith, L. Näslund, S. J. May, L. Hultman, Y. Gogotsi, P. Eklund and M. W. Barsoum, *Chem. Mater.*, 2014, **26**, 2374–2381.
67 Y. Wei, P. Zhang, R. A. Soomro, Q. Zhu and B. Xu, *Adv. Mater.*, 2021, **33**, 2103148.

68 M. Naguib, J. Halim, J. Lu, K. M. Cook, L. Hultman, Y. Gogotsi and M. W. Barsoum, *J. Am. Chem. Soc.*, 2013, **135**, 15966–15969.
69 M. Naguib and Y. Gogotsi, *Acc. Chem. Res.*, 2015, **48**, 128–135.
70 P. Urbankowski, B. Anasori, T. Makaryan, D. Er, S. Kota, P. L. Walsh, M. Zhao, V. B. Shenoy, M. W. Barsoum and Y. Gogotsi, *Nanoscale*, 2016, **8**, 11385–11391.
71 M. Li, J. Lu, K. Luo, Y. Li, K. Chang, K. Chen, J. Zhou, J. Rosen, L. Hultman, P. Eklund, P. O. Å. Persson, S. Du, Z. Chai, Z. Huang and Q. Huang, *J. Am. Chem. Soc.*, 2019, **141**, 4730–4737.
72 G. Li, L. Tan, Y. Zhang, B. Wu and L. Li, *Langmuir*, 2017, **33**, 9000–9006.
73 S. Yang, P. Zhang, F. Wang, A. G. Ricciardulli, M. R. Lohe, P. W. M. Blom and X. Feng, *Angew. Chem., Int. Ed.*, 2018, **57**, 15491–15495.
74 J. Mei, G. A. Ayoko, C. Hu, J. M. Bell and Z. Sun, *Sustainable Mater. Technol.*, 2020, **25**, e156.
75 K. Huang, Z. Li, J. Lin, G. Han and P. Huang, *Chem. Soc. Rev.*, 2018, **47**, 5109–5124.
76 Y. Li, H. Shao, Z. Lin, J. Lu, L. Liu, B. Duployer, P. O. Å. Persson, P. Eklund, L. Hultman, M. Li, K. Chen, X. Zha, S. Du, P. Rozier, Z. Chai, E. Raymundo-Piñero, P. Taberna, P. Simon and Q. Huang, *Nat. Mater.*, 2020, **19**, 894–899.
77 V. Kamysbayev, A. S. Filatov, H. Hu, X. Rui, F. Lagunas, D. Wang, R. F. Klie and D. V. Talapin, *Science*, 2020, **369**, 979–983.
78 T. Li, L. Yao, Q. Liu, J. Gu, R. Luo, J. Li, X. Yan, W. Wang, P. Liu, B. Chen, W. Zhang, W. Abbas, R. Naz and D. Zhang, *Angew. Chem., Int. Ed.*, 2018, **57**, 6115–6119.
79 G. Zou, Q. Zhang, C. Fernandez, G. Huang, J. Huang and Q. Peng, *ACS Nano*, 2017, **11**, 12219–12229.
80 W. Sun, S. A. Shah, Y. Chen, Z. Tan, H. Gao, T. Habib, M. Radovic and M. J. Green, *J. Mater. Chem. A*, 2017, **5**, 21663–21668.
81 M. R. Lukatskaya, J. Halim, B. Dyatkin, M. Naguib, Y. S. Buranova, M. W. Barsoum and Y. Gogotsi, *Angew. Chem., Int. Ed.*, 2014, **53**, 4877–4880.
82 X. Xie, Y. Xue, L. Li, S. Chen, Y. Nie, W. Ding and Z. Wei, *Nanoscale*, 2014, **6**, 11035–11040.
83 S. Pang, Y. Wong, S. Yuan, Y. Liu, M. Tsang, Z. Yang, H. Huang, W. Wong and J. Hao, *J. Am. Chem. Soc.*, 2019, **141**, 9610–9616.
84 T. Yin, Y. Li, R. Wang, O. A. Al-Hartomy, A. Al-Ghamdi, S. Wageh, X. Luo, X. Tang and H. Zhang, *Ceram. Int.*, 2021, **47**, 28642–28649.
85 H. Shi, P. Zhang, Z. Liu, S. Park, M. R. Lohe, Y. Wu, A. Shaygan Nia, S. Yang and X. Feng, *Angew. Chem., Int. Ed.*, 2021, **60**, 8689–8693.
86 W. Meng, X. Liu, H. Song, Y. Xie, X. Shi, M. Dargusch, Z. Chen, Z. Tang and S. Lu, *Nano Today*, 2021, **40**, 101273.
87 L. Verger, V. Natu, M. Carey and M. W. Barsoum, *Trends Chem.*, 2019, **1**, 656–669.
88 T. Yin, Y. Li, R. Wang, O. A. Al-Hartomy, A. Al-Ghamdi, S. Wageh, X. Luo, X. Tang and H. Zhang, *Ceram. Int.*, 2021, **47**, 28642–28649.
89 Q. Tao, M. Dahlqvist, J. Lu, S. Kota, R. Meshkian, J. Halim, J. Palisaitis, L. Hultman, M. W. Barsoum, P. O. Å. Persson and J. Rosen, *Nat. Commun.*, 2017, **8**, 14949.
90 M. Alhabeb, K. Maleski, T. S. Mathis, A. Sarycheva, C. B. Hatter, S. Uzun, A. Levitt and Y. Gogotsi, *Angew. Chem., Int. Ed.*, 2018, **57**, 5444–5448.
91 M. Alhabeb, K. Maleski, B. Anasori, P. Lelyukh, L. Clark, S. Sin and Y. Gogotsi, *Chem. Mater.*, 2017, **29**, 7633–7644.
92 B. Wang, M. Wang, F. Liu, Q. Zhang, S. Yao, X. Liu and F. Huang, *Angew. Chem., Int. Ed.*, 2020, **59**, 1914–1918.
93 M. Naguib, W. Tang, K. L. Browning, G. M. Veith, V. Maliekkal, M. Neurock and A. Villa, *ChemCatChem*, 2020, **12**, 5733–5742.
94 E. Blanco, A. Rosenkranz, R. Espinoza-González, V. M. Fuenzalida, Z. Zhang, S. Suárez and N. Escalona, *Catal. Commun.*, 2020, **133**, 105833.
95 J. Diao, M. Hu, Z. Lian, Z. Li, H. Zhang, F. Huang, B. Li, X. Wang, D. S. Su and H. Liu, *ACS Catal.*, 2018, **8**, 10051–10057.
96 J. He, P. Wu, L. Chen, H. Li, M. Hua, L. Lu, Y. Wei, Y. Chao, S. Zhou, W. Zhu and H. Li, *Chem. Eng. J.*, 2021, **416**, 129022.
97 R. Thakur, A. VahidMohammadi, J. Smith, M. Hoffman, J. Moncada, M. Beidaghi and C. A. Carrero, *ACS Catal.*, 2020, **10**, 5124–5134.
98 A. Kurlov, E. B. Deeva, P. M. Abdala, D. Lebedev, A. Tsoukalou, A. Comas-Vives, A. Fedorov and C. R. Müller, *Nat. Commun.*, 2020, **11**, 4920.
99 R. Thakur, M. Hoffman, A. VahidMohammadi, J. Smith, M. Chi, B. Tatarchuk, M. Beidaghi and C. A. Carrero, *ChemCatChem*, 2020, **12**, 3639–3643.
100 E. B. Deeva, A. Kurlov, P. M. Abdala, D. Lebedev, S. M. Kim, C. P. Gordon, A. Tsoukalou, A. Fedorov and C. R. Müller, *Chem. Mater.*, 2019, **31**, 4505–4513.
101 A. D. Dillon, M. J. Ghidiu, A. L. Krick, J. Griggs, S. J. May, Y. Gogotsi, M. W. Barsoum and A. T. Fafarman, *Adv. Funct. Mater.*, 2016, **26**, 4162–4168.
102 K. Maleski, V. N. Mochalin and Y. Gogotsi, *Chem. Mater.*, 2017, **29**, 1632–1640.
103 M. J. Gilkey and B. Xu, *ACS Catal.*, 2016, **6**, 1420–1436.
104 C. Wang, L. Wang, J. Zhang, H. Wang, J. P. Lewis and F. Xiao, *J. Am. Chem. Soc.*, 2016, **138**, 7880–7883.
105 E. Blanco, C. Sepulveda, K. Cruces, J. L. García-Fierro, I. T. Ghampson and N. Escalona, *Catal. Today*, 2020, **356**, 376–383.
106 M. M. Bhasin, J. H. McCain, B. V. Vora, T. Imai and P. R. Pujadó, *Appl. Catal., A*, 2001, **221**, 397–419.
107 B. V. Vora, *Top. Catal.*, 2012, **55**, 1297–1308.
108 M. C. Denney, V. Pons, T. J. Hebden, D. M. Heinekey and K. I. Goldberg, *J. Am. Chem. Soc.*, 2006, **128**, 12048–12049.
109 R. T. Yang, A. J. Hernández-Maldonado and F. H. Yang, *Science*, 2003, **301**, 79–81.
110 A. Rajendran, T. Cui, H. Fan, Z. Yang, J. Feng and W. Li, *J. Mater. Chem. A*, 2020, **8**, 2246–2285.
111 C. Chen and A. Bhan, *ACS Catal.*, 2017, **7**, 1113–1122.

112 M. D. Porosoff, X. Yang, J. A. Boscoboinik and J. G. Chen, *Angew. Chem., Int. Ed.*, 2014, **53**, 6705–6709.
113 J. B. Claridge, A. P. E. York, A. J. Brungs, C. Marquez-Alvarez, J. Sloan, S. C. Tsang and M. L. H. Green, *J. Catal.*, 1998, **180**, 85–100.
114 C. Shi, A. Zhang, X. Li, S. Zhang, A. Zhu, Y. Ma and C. Au, *Appl. Catal., A*, 2012, **431–432**, 164–170.
115 F. Solymosi, R. Németh, L. Óvári and L. Egri, *J. Catal.*, 2000, **195**, 316–325.
116 C. Chen and A. Bhan, *ACS Catal.*, 2017, **7**, 1113–1122.
117 M. M. Sullivan and A. Bhan, *ACS Catal.*, 2016, **6**, 1145–1152.
118 H. Bian, D. Li, S. Wang, J. Yan and S. F. Liu, *Chem. Sci.*, 2022, **13**, 1335–1341.
119 J. Chen, Y. Xu, P. Liao, H. Wang and H. Zhou, *Carbon Capture Sci. Technol.*, 2022, **4**, 100052.
120 C. Shen, K. Sun, Z. Zhang, N. Rui, X. Jia, D. Mei and C. Liu, *ACS Catal.*, 2021, **11**, 4036–4046.
121 Y. Xu, C. Luo, H. Sang, B. Lu, F. Wu, X. Li and L. Zhang, *Chem. Eng. J.*, 2022, **435**, 134960.
122 H. Zhou, Z. Chen, A. V. López, E. D. López, E. Lam, A. Tsoukalou, E. Willinger, D. A. Kuznetsov, D. Mance, A. Kierzkowska, F. Donat, P. M. Abdala, A. Comas-Vives, C. Copéret, A. Fedorov and C. R. Müller, *Nat. Catal.*, 2021, **4**, 860–871.
123 D. S. Newsome, *Catal. Rev.*, 1980, **21**, 275–318.
124 C. Ratnasamy and J. P. Wagner, *Catal. Rev.*, 2009, **51**, 325–440.
125 J. A. Rodriguez, S. Ma, P. Liu, J. Hrbek, J. Evans and M. Pérez, *Science*, 2007, **318**, 1757–1760.
126 R. Thakur, M. Hoffman, A. VahidMohammadi, J. Smith, M. Chi, B. Tatarchuk, M. Beidaghi and C. A. Carrero, *Chemcatchem*, 2020, **12**, 3639–3643.
127 T. Zambelli, J. Wintterlin, J. Trost and G. Ertl, *Science*, 1996, **273**, 1688–1690.
128 K. Han, X. Zhang, P. Deng, Q. Jiao and E. Chu, *Vacuum*, 2020, **180**, 109572.
129 J. D. Gouveia, Á. Morales-García, F. Viñes, F. Illas and J. R. B. Gomes, *Appl. Catal., B*, 2020, **260**, 118191.
130 Y. Zhang, X. Zhang, C. Cheng and Z. Yang, *Chin. Chem. Lett.*, 2020, **31**, 931–936.
131 Y. Wang, J. Wang, G. Han, C. Du, Q. Deng, Y. Gao, G. Yin and Y. Song, *Ceram. Int.*, 2019, **45**, 2411–2417.
132 G. Bharath, K. Rambabu, A. Hai, I. Othman, N. Ponpandian, F. Banat and P. Loke Show, *Chem. Eng. J.*, 2021, **414**, 128869.
133 M. Sankar, Q. He, R. V. Engel, M. A. Sainna, A. J. Logsdail, A. Roldan, D. J. Willock, N. Agarwal, C. J. Kiely and G. J. Hutchings, *Chem. Rev.*, 2020, **120**, 3890–3938.
134 J. Ma, Q. Jiang, Y. Zhou, W. Chu, S. Perathoner, C. Jiang, K. H. Wu, G. Centi and Y. Liu, *Small*, 2021, **17**, 2007509.
135 D. Zhao, Z. Chen, W. Yang, S. Liu, X. Zhang, Y. Yu, W. Cheong, L. Zheng, F. Ren, G. Ying, X. Cao, D. Wang, Q. Peng, G. Wang and C. Chen, *J. Am. Chem. Soc.*, 2019, **141**, 4086–4093.
136 Z. Li, L. Yu, C. Milligan, T. Ma, L. Zhou, Y. Cui, Z. Qi, N. Libretto, B. Xu, J. Luo, E. Shi, Z. Wu, H. Xin, W. N. Delgass, J. T. Miller and Y. Wu, *Nat. Commun.*, 2018, **9**, 5258.
137 Z. Li, Y. Cui, Z. Wu, C. Milligan, L. Zhou, G. Mitchell, B. Xu, E. Shi, J. T. Miller, F. H. Ribeiro and Y. Wu, *Nat. Catal.*, 2018, **1**, 349–355.
138 Z. Li, Y. Xiao, P. R. Chowdhury, Z. Wu, T. Ma, J. Z. Chen, G. Wan, T. Kim, D. Jing, P. He, P. J. Potdar, L. Zhou, Z. Zeng, X. Ruan, J. T. Miller, J. P. Greeley, Y. Wu and A. Varma, *Nat. Catal.*, 2021, **4**, 882–891.
139 L. D. Pachón and G. Rothenberg, *Appl. Organomet. Chem.*, 2008, **22**, 288–299.
140 N. Yan, C. Xiao and Y. Kou, *Coord. Chem. Rev.*, 2010, **254**, 1179–1218.
141 M. Liu, Z. Lyu, Y. Zhang, R. Chen, M. Xie and Y. Xia, *Nano Lett.*, 2021, **21**, 2248–2254.
142 W. A. Spieker and J. R. Regalbuto, *Chem. Eng. Sci.*, 2001, **56**, 3491–3504.
143 Q. Chen, W. Jiang and G. Fan, *Dalton Trans.*, 2020, **49**, 14914–14920.
144 T. K. Slot, F. Yue, H. Xu, E. V. Ramos-Fernandez, A. Sepúlveda-Escribano, Z. Sofer, G. Rothenberg and N. R. Shiju, *2D Mater.*, 2020, **8**, 15001.
145 T. Liu, Z. Zhang, L. Yan, Z. Zhang, Y. Zhang and Y. Yin, *Int. J. Hydrogen Energy*, 2021, **46**, 33098–33106.
146 J. Liu, H. Xiao and J. Li, *J. Am. Chem. Soc.*, 2020, **142**, 3375–3383.
147 V. Ramalingam, P. Varadhan, H. C. Fu, H. Kim, D. Zhang, S. Chen, L. Song, D. Ma, Y. Wang, H. N. Alshareef and J. H. He, *Adv. Mater.*, 2019, **31**, 1903841.
148 Y. Yan, H. Cheng, Z. Qu, R. Yu, F. Liu, Q. Ma, S. Zhao, H. Hu, Y. Cheng, C. Yang, Z. Li, X. Wang, S. Hao, Y. Chen and M. Liu, *J. Mater. Chem. A*, 2021, **9**, 19489–19507.
149 X. Wu, H. Zhang, S. Zuo, J. Dong, Y. Li, J. Zhang and Y. Han, *Nano-Micro Lett.*, 2021, **13**, 1–28.
150 N. Cheng, S. Stambula, D. Wang, M. N. Banis, J. Liu, A. Riese, B. Xiao, R. Li, T. Sham, L. Liu, G. A. Botton and X. Sun, *Nat. Commun.*, 2016, **7**, 13638.
151 X. Zhang, J. Lei, D. Wu, X. Zhao, Y. Jing and Z. Zhou, *J. Mater. Chem. A*, 2016, **4**, 4871–4876.
152 C. Cheng, X. Zhang, M. Wang, S. Wang and Z. Yang, *Phys. Chem. Chem. Phys.*, 2018, **20**, 3504–3513.
153 B. L. Mojet, J. T. Miller, D. E. Ramaker and D. C. Koningsberger, *J. Catal.*, 1999, **186**, 373–386.
154 S. Zhao, Y. Kang, M. Liu, B. Wen, Q. Fang, Y. Tang, S. He, X. Ma, M. Liu and Y. Yan, *J. Mater. Chem. A*, 2021, **9**, 18927–18946.